A chemo-mechanical model coupling damage and mechanofluorescence for tough interpenetrating elastomers

Peng Sun[a], Mokarram Hossain[b], Paul Steinmann[c,d], Rui Xiao[a,*]

[a] *State Key Laboratory of Fluid Power and Mechatronic Systems, Department of Engineering Mechanics, Zhejiang University, Hangzhou 310027, China*

[b] *Zienkiewicz Institute for Modelling, Data and AI, Faculty of Science and Engineering, Swansea University, Swansea, SA1 8EN, United Kingdom*

[c] *Institute of Applied Mechanics, Friedrich-Alexander-Universität Erlangen-Nürnberg, 91058 Erlangen, Germany*

[d] *Glasgow Computational Engineering Centre, School of Engineering, University of Glasgow, G12 8QQ, United Kingdom*

Abstract

Mechanochemical probes have emerged as powerful tools for directly visualizing stress distribution and damage evolution in polymeric materials. Recent studies have successfully embedded rhodamine-based mechanophores into multiple network elastomers to enable high-resolution mechanofluorescent signaling. However, cyclic loading experiments reveal distinct fluorescence response across different loading cycles, which indicate a strong coupling between mechanofluorescent signals and the progressive damage within polymer networks. Motivated by these findings, we develop a chemo-mechanical model that quantitatively captures the mechanofluorescent behavior. We first introduce an extended-Langevin model for the behavior of single chain with deformable bonds. The free energy density of the first network is derived by considering chains with varying segment lengths, while a kinetic damage evolution law is introduced to account for progressive network degradation. The free energy density of multiple network elastomers is formulated as the combined contribution of a hyperelastic matrix network and a first network undergoing damage evolution. We further incorporate the chemical kinetics of ring-opening mechanophores into the theoretical framework. Activation of mechanophores occurs when the chain force exceeds a critical threshold, while deactivation occurs upon a reduction or removal of the force. Through parametric analysis, we demonstrate the key factors that strongly influence mechanochemical behavior. The model is then validated against experimental results from mechanofluorescent multiple network elastomers, accurately capturing both mechanical and fluorescent response in single to triple network

*Corresponding author.
Email address: rxiao@zju.edu.cn (Rui Xiao)

elastomers under cyclic loading. Notably, the model reproduces stress softening and the increase in critical activation stretch caused by accumulated damage. The model is further implemented for finite element analysis to predict cyclic mechanochemical response under inhomogeneous deformation conditions, with predictions showing quantitative consistency with experimental spatial fluorescence distribution.
Keywords: Mechanofluorescent elastomers; chemo-mechanical model; damage behavior; ring-opening mechanophores.

---

1. Introduction

Mechanophores are force-sensitive molecular units that undergo chemical reactions when subjected to external mechanical stimuli, which hold great promise for developing biomedical devices (Wang et al. 2017, 2014, Barbee et al. 2018), force sensors (Cho et al. 2017, Chen et al. 2020), damage detection systems (Ducrot et al. 2014, Ju et al. 2023, Li et al. 2022), and self-strengthening materials (Matsuda et al. 2019, Wang et al. 2025, 2021). Recently, mechanochemically responsive polymers have been developed by covalently incorporating mechanophores into polymer networks (Chen et al. 2021a, Li et al. 2018, Wang et al. 2015a). Upon the application of external loading, polymer chains transmit the mechanical force to these mechanophores, thereby triggering their chemical activation to emit optical signals. Through the use of optical imaging and spectroscopic analysis, the resulting optical signals can be quantitatively measured, enabling the visualization of the internal stress distribution and damage evolution within the materials at the microscale. Two main types of mechanophores are widely used: one based on chain-scission mechanisms, such as dioxetane and pi-extended anthracenes (Chen et al. 2012, Göstl and Sijbesma 2016), and the other relying on ring-opening reactions (non-scission), such as spiropyran and rhodamine derivatives (Davis et al. 2009, Wang et al. 2015b).

scission mechanophores reversibly break into two fragments under high mechanical forces, emitting chemiluminescence (Chen et al. 2012) or becoming fluorescent (Göstl and Sijbesma 2016). Since the optical signals are directly related to the number of fractured chains, these mechanophores are well-suited for probing microscopic damage. They have been integrated into various material systems—such as hydrogels, polydimethylsiloxane (PDMS), and other elastomers—to understand damage and fracture behaviors (Li et al. 2022, Clough et al. 2016, Ducrot et al. 2014, Ju et al. 2023). For example, Ducrot et al. (2014) visualized damage at the crack tip in elastomers by incorporating dioxetane into multiple network elastomers, revealing that the toughening effect originates from the rupture of sacrificial bonds. Based on this mechanism, Sun et al. (2024) proposed a micromechanical model that quantitatively captures the mechanical and mechanoluminescent response of double to quadruple network elastomers, successfully predicting

damage under inhomogeneous deformation. Similarly, Lavoie et al. (2019) developed a continuum framework for capturing the coupled stress and damage response of multiple network elastomers, calibrated using mechanoluminescent data. It should be noted that the complex synthetic procedures required for such mechanosensitive moieties partially restrict their broad applicability. Furthermore, given the transient nature of their chemiluminescence or the inherently low intensity of their fluorescence, the detection and quantitative characterization of the associated signals remain highly challenging.

In contrast, non-scissile mechanophores such as spiropyran and rhodamine derivatives can be synthesized through comparatively simple procedures. Additionally, they undergo ring-opening isomerization under a critical force, which is accompanied by persistent and ultrasensitive color changes or fluorescence response (Davis et al. 2009, Beiermann et al. 2014, Li et al. 2018, Wang et al. 2015b, Wu et al. 2022, Jiang et al. 2025). Davis et al. (2009) pioneered a mechanochemical approach by incorporating spiropyran units into polymer networks to achieve mechanochromism. In addition, Wang et al. (2015b) introduced rhodamine into polyurethanes to realize compression-induced chromism. Chen et al. (2020) mapped the stress distribution by correlating the chromatic changes of spiropyran-crosslinked multiple network elastomers with the applied stress, and demonstrated that the optical signals are closely related to the local stress values. Since then, many non-scissile mechanophores have been applied for stress sensors, electro-mechano-chemical devices, and soft robotics (Cho et al. 2017, Wang et al. 2014, Gossweiler et al. 2015). To model the chemo-mechanical coupling effect, Silberstein et al. (2013, 2014) proposed theoretical frameworks for the activation of spiropyran in elastomer matrices. Wang et al. (2015a) introduced a hyperelastic model that effectively quantified the stress-fluorescence behavior in PDMS films. However, neither of these models considered the influence of damage on mechanochemical response. Recently, Wang et al. (2017) synthesized a novel rhodamine-based mechanophore and successfully incorporated it into multiple network elastomers, enabling robust mechanofluorescent signaling. Experimental studies revealed substantial polymer chain scission under mechanical loading for interpenetrating network system (Ducrot et al. 2014). However, the relationship between the mechanofluorescent response and the underlying damage mechanisms, such as bond rupture kinetics, remains poorly understood.

In this study, we aim to investigate the influence of damage on mechanofluorescent behavior and also develop a chemo-mechanical model to describe mechanofluorescence in tough elastomers. Since multiple network elastomers are typical tough materials and they have the apparent damage mechanism, we conduct loading and reloading tests to characterize the mechanical and mechanochemical response for multiple network elastomers with non-scissile mechanophores. Different from the scission mechanophores, the optical response of non-scission mechanophores is indirectly coupled to damage evolution, resulting in a more complex chemo-mechanical response. The novelty of the present work lies in the development of a constitutive model to describe the relationship of the fluorescence and damage behavior,

which is distinct from our previous works (Xiao et al. 2021, Sun et al. 2024). The paper is organized as follows. Section 2 presents the experimental observations for rhodamine-based mechanofluorescent elastomers. Motivated by these findings, a constitutive model is then developed. A parameter study is then performed in Sections 4, followed by parameter calibration procedure. Finally, the model is validated against mechanical and fluorescence response under both homogeneous and inhomogeneous deformation conditions. The paper ends with conclusions.

2. Experimental methods

2.1. Material Preparation

Mechanofluorescent multiple network elastomers were synthesized through a multi-step photopolymerization process. The process began with the fabrication of the first (single) network containing mechanophores. A precursor solution was prepared by mixing 2.25 mL (20.7 mmol) of ethyl acrylate (EA) monomer, 146 mg (1 mol% relative to the monomer) of a rhodamine-based mechanophore cross-linker, 15 mg (0.3 mol%) of the photoinitiator 2-hydroxy-4'-(2-hydroxyethoxy)-2-methylpropiophenone (I2959), and 2.25 mL of ethyl acetate as the solvent. The mixture was thoroughly stirred and cast into a glass mold using a syringe. The mold was exposed to ultraviolet (UV) light for one hour in a UV crosslinking chamber (CL-3000L). After photopolymerization, the resulting single network (SN) elastomer was subjected to solvent evaporation until its mass stabilized. To fabricate multiple network elastomers, the dried single-network sample was swollen in a second precursor solution for matrix network formation. This solution contained 30 mL (276 mmol) of EA monomer, 10.5 μL (0.02 mol%) of butanediol diacrylate (BDA) as a cross-linker, and 200 mg (0.3 mol%) of I2959. The swollen elastomer was again exposed to UV light to induce polymerization and form a loosely cross-linked matrix network. Repeating the swelling and polymerization steps yielded double network (DN) and triple network (TN) elastomers, depending on the number of matrix layers introduced.

In this work, the term "matrix network" is used to collectively represent the subsequently introduced second and third networks. These networks possess similar roles in the material system, characterized by much lower crosslinking densities than the first network, and they are fully interpenetrated with the first network rather than existing as independent or discrete phases. The terms double network and triple network elastomers refer to elastomers with sequentially introduced, interpenetrating polymer networks during synthesis, and do not imply mechanical or structural independence among the individual networks.

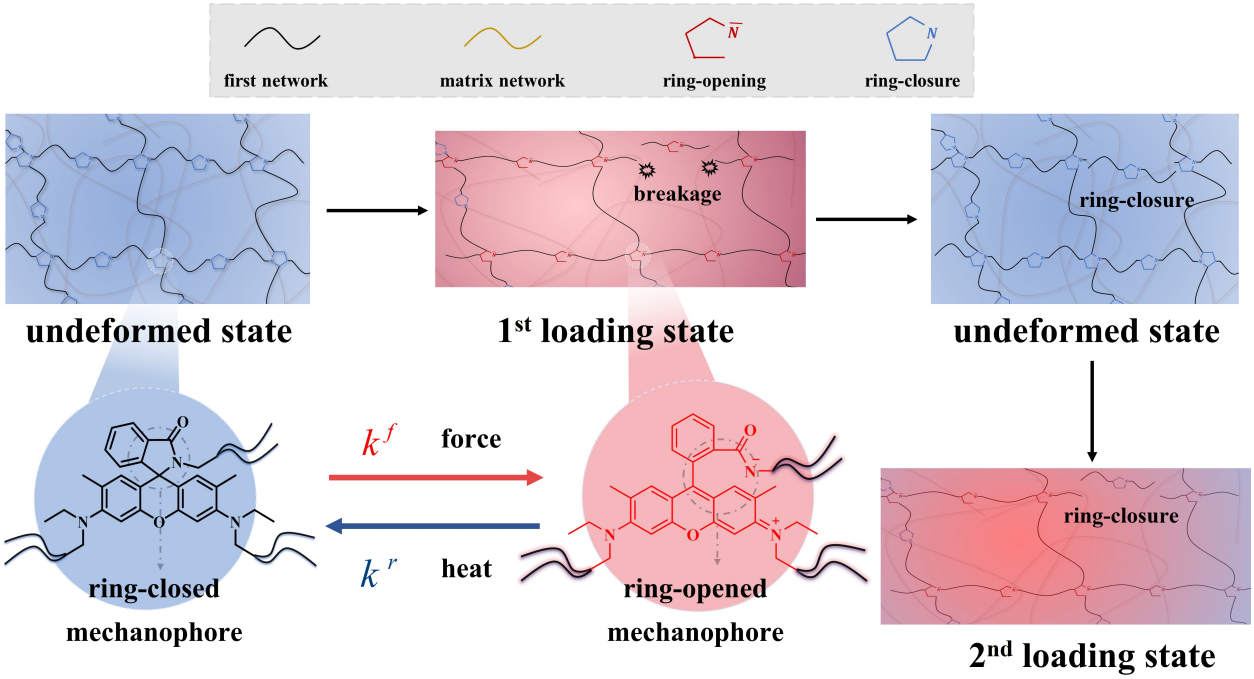

Figure 1: Schematic illustration of fluorescence and damage evolution for elastomers in loading and reloading tests. The observed fluorescence attenuation originates from the ring-closure of mechanophores crosslinked onto the damaged chains.

The chemical structure of the rhodamine-based mechanophore (TAR), originally synthesized by Wang et al. (2017), is shown in Fig. 1. Upon a critical mechanical force, these mechanophores undergo a ring-opening reaction, resulting in the emission of red fluorescence. This process is reversible, and the mechanophores can return to their ring-closed, non-fluorescent state as the force is decreased to the threshold value. The molar ratio of mechanophore to monomer in the first network was fixed at 1 mol% for all samples. A summary of the elastomer compositions is provided in Table 1. Due to the swelling during matrix incorporation, the volume fraction of the first network, denoted by φ_1, decreases and can be calculated using the following relation:

$$\varphi_1 = \frac{1}{\lambda_{s1}^3}, \tag{1}$$

where λ_{s1} is the pre-stretching ratio of the first network, determined by the ratio of the final thickness of the multiple network elastomer to that of the single network elastomer. Our experimentally measured values of λ_{s1} and φ_1 are consistent with those reported in Wang et al. (2017).

Table 1: Summary of material compositions.

Type of network	TAR in first network (mol%)	λ_{s1}	first network wt% (φ_1)	Tag
Single network	1	1.0	100.0	SN
Double network	1	1.6	24.4	DN
Triple network	1	2.4	7.2	TN

2.2. Mechanical characterization

Following synthesis, various multiple network elastomers were shaped into dog-bone specimens (gauge width: 2 mm, gauge length: 25 mm) by a laser cutter (Chan Xan, CW-530) to evaluate homogeneous deformation. Loading and reloading tests were performed at strain rates of 0.05 /s and 0.001 /s. The measurements were carried out on an electromechanical machine (SANS, CMT6103) equipped with a 200 N load cell. It is noted that the loading and reloading tests refer to two independent loading-unloading experiments performed on the same specimen rather than the conventional continuous loading-unloading and reloading modes. Since we need to record the fluorescence signals in two loading cycles, it is necessary to reset the fluorescence response before the second test. Based on previous experimental observations (Wang et al. 2017), resting the specimen at room temperature for 4 hours is sufficient to eliminate fluorescence without affecting the mechanical response of the elastomers. Therefore, after the first test, the specimen was rested at room temperature for 4 hours before conducting the second loading–unloading experiment. Additionally, considering that accurate characterization of the fluorescence response during the unloading phase is challenging due to blue-shift phenomenon (Wang et al. 2017, Sun et al. 2025), we have deliberately excluded the discussion of mechanical and mechanochemical responses during unloading from the current study.

2.3. Fluorescent characterization

Under mechanical loading, the mechanochemically responsive elastomers exhibit fluorescence when exposed to ultraviolet (UV) light. To monitor this response during tensile testing, we developed an in-situ fluorescence characterization system. The basic principle involves the sample under tension emitting fluorescence upon UV irradiation at an excitation wavelength of 365 nm. The emitted signals were captured by an industrial RGB camera (BFS-U3-123S6C-C) fitted with a 590–620 nm filter. The filter selection was based on the fluorescence emission spectrum of the deformed elastomers. Before experiments, the camera was calibrated by adjusting the white balance (red channel: 1.89, blue

channel: 2.21). Throughout the tests, the exposure time was set to 50 milliseconds, and the gain was fixed at 25. Fluorescence intensity was quantified using an intensity analysis method, which collects optical signals in the selected wavelength range (590–620 nm) and calculates the grayscale value per pixel for the regions of interest in the captured images. A thickness correction procedure was also applied to this method. It should be noted that prolonged ultraviolet exposure can induce photodegradation of the elastomeric network. To minimize this effect, particularly in experiments conducted at low strain rates, we adopted an intermittent illumination protocol. Specifically, the UV light source was switched on only every 30 seconds to record fluorescence images, thereby significantly reducing the total exposure time. Control experiments confirmed that this intermittent UV illumination does not affect the measured mechanical response of the elastomer.

2.4. Experimental observation

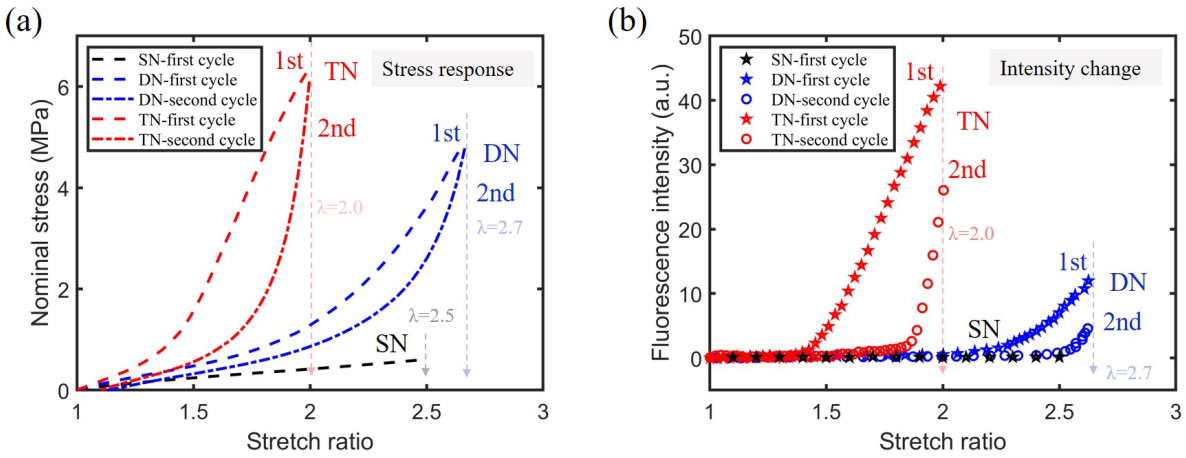

Figure 2: The comparison of SN, DN, and TN elastomers in uniaxial loading and reloading tests: (a) stress response and (b) fluorescence intensity change. Owing to the low stress level, the SN elastomer remains non-fluorescent. The fluorescence response of both DN and TN elastomers in the second loading cycle is weaker than that observed in the first cycle. The experimental data were extracted from Sun et al. (2025).

We plot the stress response and corresponding fluorescence intensities for SN, DN, and TN elastomers subjected to uniaxial cyclic loading with maximum stretch ratios of 2.5, 2.7, and 2.0, respectively, as shown in Fig. 2. The SN elastomer exhibits low stress levels and negligible fluorescence activation, indicating minimal mechanochemical activity. In contrast, the DN elastomer displays pronounced strain hardening at large deformations during the first loading cycle, accompanied by notable fluorescence emission. In the second cycle, the DN elastomer exhibits mechanical softening, while fluorescence activation becomes both delayed and attenuated compared to the first cycle. It is widely recognized that in multiple network systems, increasing the number of interpenetrating networks enhances material toughness, increases energy dissipation, and promotes damage accumulation within the first network under deformation (Ducrot et al. 2014). Consistent with this understanding, for TN elastomer, both the onset of strain hardening and

the fluorescence activation threshold occur at smaller stretches compared to the DN elastomer. Notably, the reduction in fluorescence intensity and the corresponding degradation in mechanical response between successive loading cycles are significantly more pronounced in TN elastomers than in DN elastomers.

To better elucidate these experimental findings, Fig. 1 schematically illustrates the progression of fluorescence and network degradation in the loading and reloading tests. During the initial loading, mechanofluorescence is activated via ring-opening reactions of rhodamine-based mechanophores covalently embedded in two distinct polymer chain populations within the first network. Fluorescence emission arises from both undamaged chains and those undergoing bond scission or irreversible network damage. Upon unloading, as the specimen returns to its undeformed state, the mechanophores revert to their ring-closed (non-fluorescent) configuration. During subsequent reloading, fluorescence is generated exclusively from mechanophores on the remaining intact chains, as mechanophores on previously damaged chains are no longer mechanically active. This mechanism accounts for the diminished fluorescence intensity observed during the second loading cycle. Besides, in this elastomer system, damage is primarily governed by irreversible chain scission in the first network, which results in very limited self-recovery capability (Webber et al. 2007). These results underscore a strong coupling between fluorescence response and damage accumulation within the polymer network, serving as the primary motivation for developing a chemo-mechanical constitutive model to quantitatively capture this interaction.

3. Theory

In this section, a constitutive model is formulated for mechanofluorescent multiple network elastomers. We first introduce the mechanical framework, including the free energy of a single chain, the overall free-energy density of the system, and the governing equations for damage evolution. Next, we incorporate the chemical kinetics of ring-opening mechanophores by using the chain force as the coupling parameter linking mechanical and chemical processes. Finally, we quantify the mechanochemical response by postulating that the macroscopic fluorescence intensity scales linearly with the concentration of activated mechanophores, thereby bridging molecular-scale activation events with bulk optical properties.

3.1. The single chain model

The classical single-chain model based on Langevin statistics has been widely used to characterize the strain-stiffening behavior of rubber-like materials. Nevertheless, recent studies (Lavoie et al. 2019, Xiao et al. 2021, Sun et al. 2024) have demonstrated that this single-chain model is unsuitable for describing the stress–strain response of multiple network elastomers because the model fails to account the response of single chains when approaching the finite extensibility limit.

To overcome this limitation, several works (Xiao et al. 2021, Sun et al. 2024) adopted the extended Langevin model originally proposed by Mao et al. (2017), which incorporates bond deformation. In this formulation, the total stretch of a polymer chain is expressed as the product of two multiplicative components: the bond stretch λ^{b} and the stretch caused by configuration rearrangement λ^{c}, giving $\lambda = \lambda^{\mathrm{b}}\lambda^{\mathrm{c}}$. This theoretical extension is further supported by experimental evidence from Wang et al. (2021), who reported substantial bond elongation under single-chain tensile loading. These findings provide strong justification for incorporating the competitive interplay between entropic elasticity and bond deformation into the constitutive modeling of network elastomers. The single-chain free energy $w^{\mathrm{ext}} = w^{\mathrm{ext}}(\lambda, \lambda^{\mathrm{b}})$ of the extended Langevin chain model is given as:

$$w^{\mathrm{ext}} = kTN\left[\frac{\lambda}{\lambda^{\mathrm{b}}\sqrt{N}}\beta + \ln\frac{\beta}{\sinh\beta}\right] + \frac{1}{2}NE_{\mathrm{b}}\ln^2(\lambda^{\mathrm{b}}) + \text{constant}, \quad \beta = \mathscr{L}^{-1}\left(\frac{\lambda}{\lambda^{\mathrm{b}}\sqrt{N}}\right), \tag{2}$$

where k denotes the Boltzmann constant, T the absolute temperature, N the number of chain segments, λ the stretch ratio, β the inverse function of the Langevin function, and E_{b} the bond stiffness. λ is defined as $\lambda = r/[\sqrt{N}b]$, where r is the end-to-end distance of the chain and b is the Kuhn length. The Langevin function is expressed as $\mathscr{L}(x) = \coth x - 1/x$. We employ the inverse Langevin approximation proposed by Kroeger (2015), given by $\mathscr{L}^{-1}(x) = 3x/[[1-x^2][1+\frac{1}{2}x^2]]$.

The bond deformation λ^{b} is obtained by minimizing the single-chain free energy:

$$\frac{\partial w^{\mathrm{ext}}(\lambda, \lambda^{\mathrm{b}})}{\partial \lambda^{\mathrm{b}}} = 0, \tag{3}$$

and it further leads to

$$\overline{E}\ln\lambda^{\mathrm{b}} = \frac{\lambda}{\lambda^{\mathrm{b}}\sqrt{N}}\beta, \quad \overline{E} = \frac{E_{\mathrm{b}}}{kT}, \tag{4}$$

where $\overline{E}$ denotes the normalized bond stiffness.

The chain force f, can be obtained as (Wang et al. 2015a, Xiao et al. 2021)

$$f = \frac{\partial w^{\text{ext}}}{\partial r} = \frac{kT}{b}\frac{\beta}{\lambda^{\text{b}}}, \tag{5}$$

where r is the end-to-end distance of the chain and b is the Kuhn length. Since kT/b is a constant, the chain force can be further normalized as:

$$\overline{f} = \frac{fb}{kT} = \frac{\beta}{\lambda^{\text{b}}}. \tag{6}$$

3.2. Constitutive relation

Multiple network elastomers typically comprise two distinct components: a brittle first network (consisting of short, highly pre-stretched polymer chains) and a soft matrix network (comprising longer, less-stretched polymer chains). Consequently, the overall free energy density is typically represented as the combined contribution from the two networks. We first focus on formulating the free energy density of the first network. Due to the inherent randomness in crosslinking or polymerization, the chains in a polymer network display a broad distribution of lengths. Here, we assume that the first network consists of M subnetworks, each comprising chains of identical length (Wang et al. 2015a). The chain density fraction of the jth subnetwork within the first network is then given by

$$P_j = \frac{n_j}{n_{\text{f}}}, \quad j = 1, ..., M, \tag{7}$$

where $n_{\text{f}} = \sum_j n_j$ denotes the total number of polymer chains, and n_j represents the number of chains with N_j segments.

Through incorporating the extended single-chain model, the first-network free energy density W^{f} is then written as (Xiao et al. 2021):

$$W^{\text{f}} = \varphi_1 n_{\text{f}} kT \sum_j P_j N_j \left[\frac{\lambda}{\lambda_j^{\text{b}}\sqrt{N_j}}\beta_j + \ln\frac{\beta_j}{\sinh\beta_j} + \frac{1}{2}\overline{E}\ln^2(\lambda_j^{\text{b}}) \right], \quad \beta_j = \mathscr{L}^{-1}\left(\frac{\lambda}{\lambda_j^{\text{b}}\sqrt{N_j}}\right), \tag{8}$$

where φ_1 denotes the volumetric fraction of the first network. As shown in Table 1, φ_1 decreases with increasing network order due to the formation of additional matrix networks (Eq. 1).

The high toughness of multiple network elastomers arises from the fracture of the first network, which acts as sacrificial bonds (Ducrot et al. 2014). Therefore, chains within the first network must follow a damage evolution rule detailed in the following subsection. In contrast, Chen et al. (2021b) demonstrated via spiropyran mechanochemistry that the first

network predominantly bears the mechanical load prior to necking in single, double, and triple network elastomers. Focusing on the pre-necking regime, the matrix network contribution is comparatively minor. Accordingly, the matrix is described through a hyperelastic formulation, with the free energy density W^{m} given by

$$W^{\mathrm{m}} = [1-\varphi_{\mathrm{l}}]\, n_{\mathrm{m}} kT N_{\mathrm{m}} \left[\frac{\lambda}{\sqrt{N_{\mathrm{m}}}} \beta_{\mathrm{m}} + \ln \frac{\beta_{\mathrm{m}}}{\sinh \beta_{\mathrm{m}}} \right], \quad \beta_{\mathrm{m}} = \mathscr{L}^{-1}\left(\frac{\lambda}{\sqrt{N_{\mathrm{m}}}} \right), \tag{9}$$

where N_{m} and n_{m} denote the number of chain segments and the total number of polymer chains in the matrix network, respectively. Given the long chain nature of the matrix network, N_{m} takes a comparatively large value.

To link single-chain deformation with macroscopic deformation, various micro-macro transition schemes have been proposed (Khiêm and Itskov 2016, Zhan et al. 2023b, Arruda and Boyce 1993). Among these, the eight-chain network model (Arruda and Boyce 1993) balances simplicity with accuracy. In this model, the equivalent chain stretch is given by:

$$\overline{\lambda} = \sqrt{\frac{I_1(\mathbf{C})}{3}}, \tag{10}$$

where I_1 is the first invariant of the right Cauchy-Green deformation tensor $\mathbf{C} = \mathbf{F}^{\mathrm{T}}\mathbf{F}$, with $\mathbf{F}$ being the deformation gradient. For isotropically prestretched first networks, the equivalent stretch generalizes to:

$$\widetilde{\lambda} = \lambda_{\mathrm{s1}} \sqrt{\frac{I_1(\mathbf{C})}{3}}, \tag{11}$$

where λ_{s1} is the first network prestretching ratio as defined in Table 1. Here the free energy density is constructed based on the eight-chain model. It should be noted that various other hyperelastic models have been developed in recent years (Anssari-Benam et al. 2022b,a, Zhan et al. 2023b), which can also well capture the behavior of soft materials.

The total free energy density W of the multiple network elastomer is expressed as:

$$\begin{aligned} W &= W^{\mathrm{f}} + W^{\mathrm{m}} \\ &= \varphi_{\mathrm{l}} G_{\mathrm{f}} \sum_j P_j N_j \left[\frac{\widetilde{\lambda}}{\lambda_j^{\mathrm{b}} \sqrt{N_j}} \beta_j + \ln \frac{\beta_j}{\sinh \beta_j} + \frac{1}{2} \overline{E} \ln^2 (\lambda_j^{\mathrm{b}}) \right] + [1-\varphi_{\mathrm{l}}]\, G_{\mathrm{m}} N_{\mathrm{m}} \left[\frac{\overline{\lambda}}{\sqrt{N_{\mathrm{m}}}} \beta_{\mathrm{m}} + \ln \frac{\beta_{\mathrm{m}}}{\sinh \beta_{\mathrm{m}}} \right], \\ \beta_j &= \mathscr{L}^{-1}\left(\frac{\widetilde{\lambda}}{\lambda_j^{\mathrm{b}} \sqrt{N_j}} \right), \quad \beta_{\mathrm{m}} = \mathscr{L}^{-1}\left(\frac{\overline{\lambda}}{\sqrt{N_{\mathrm{m}}}} \right), \end{aligned} \tag{12}$$

where $G_{\mathrm{f}} = n_{\mathrm{f}} kT$ and $G_{\mathrm{m}} = n_{\mathrm{m}} kT$ represent the shear moduli of the first and matrix networks, respectively. Under the

assumption of incompressibility, the Cauchy stress is then obtained as:

$$\boldsymbol{\sigma} = 2\mathbf{F}\frac{\partial W}{\partial \mathbf{C}}\mathbf{F}^{\mathrm{T}} + p\mathbf{I}, \tag{13}$$

where p is the hydrostatic pressure to enforce incompressibility and $\mathbf{I}$ denotes the identity tensor.

Substituting Eq. (12) into Eq. (13), the Cauchy stress can be calculated using the following chain rule,

$$\boldsymbol{\sigma} = 2\mathbf{F}[\frac{\partial W^{\mathrm{f}}}{\partial \widetilde{\lambda}}\frac{\partial \widetilde{\lambda}}{\partial \mathbf{C}} + \frac{\partial W^{\mathrm{f}}}{\partial \beta_j}\frac{\partial \beta_j}{\partial \mathbf{C}} + \frac{\partial W^{\mathrm{m}}}{\partial \overline{\lambda}}\frac{\partial \overline{\lambda}}{\partial \mathbf{C}} + \frac{\partial W^{\mathrm{m}}}{\partial \beta_{\mathrm{m}}}\frac{\partial \beta_{\mathrm{m}}}{\partial \mathbf{C}}]\mathbf{F}^{\mathrm{T}} + p\mathbf{I}. \tag{14}$$

Finally, it leads to the following form for the Cauchy stress:

$$\boldsymbol{\sigma} = \varphi_1 \sum_j P_j \frac{G_{\mathrm{f}}\sqrt{N_j}}{3}\frac{\lambda_{\mathrm{s1}}^2}{\widetilde{\lambda}}\frac{\beta_j}{\lambda_j^{\mathrm{b}}}\mathbf{b} + [1-\varphi_1]\frac{G_{\mathrm{m}}\sqrt{N_{\mathrm{m}}}}{3}\frac{\beta_{\mathrm{m}}}{\overline{\lambda}}\mathbf{b} + p\mathbf{I}, \tag{15}$$

where $\mathbf{b} = \mathbf{F}\mathbf{F}^{\mathrm{T}}$ is the left Cauchy-Green deformation tensor.

For homogeneous and incompressible uniaxial deformation, the deformation gradient is given by:

$$\mathbf{F} = \lambda_1 \mathbf{e_1}\otimes\mathbf{e_1} + \frac{1}{\sqrt{\lambda_1}}\mathbf{e_2}\otimes\mathbf{e_2} + \frac{1}{\sqrt{\lambda_1}}\mathbf{e_3}\otimes\mathbf{e_3}, \tag{16}$$

where λ_1 is the principal stretch in the loading direction and $\{\mathbf{e_1}, \mathbf{e_2}, \mathbf{e_3}\}$ are the orthonormal basis vectors with $\mathbf{e_1}$ taken along the loading direction. The Cauchy stress component σ_1 is obtained by enforcing the transverse stress-free condition ($\sigma_2 = 0$) to eliminate p. The corresponding nominal stress τ_1 is calculated as:

$$\tau_1 = \frac{\sigma_1}{\lambda_1}. \tag{17}$$

3.3. Damage evolution

The first network needs to satisfy appropriate damage evolution criteria. To model the stress softening effect induced by damage (often referred to as the Mullins effect), a variety of constitutive models have been proposed (Zhao et al. 2021, Vernerey et al. 2018, Buche and Silberstein 2021, Zhan et al. 2023a, Lavoie et al. 2019, Wang et al. 2024, Sun et al. 2024, You et al. 2025). These models typically employ two main approaches: the network alteration theory

(Marckmann et al. 2002) and the bond rupture theory (Dargazany and Itskov 2009, Lavoie et al. 2016, Lei and Liu 2024). The bond rupture theory assumes that the material comprises polymer chains with a broad length distribution, where shorter chains rupture first under external loading, followed by longer chains.

In the current study, the bond-rupture theory is employed as the damage criterion because it effectively captures the damage behavior of multiple network elastomers (Lavoie et al. 2016, 2019, Sun et al. 2024). Moreover, since our recent experiments show that the damage evolution in TN elastomers exhibits slightly time-dependent characteristics, we modify the rate-dependent damage model proposed by Lavoie et al. (2016) by introducing a damage criterion, expressed as

$$\frac{dP_j}{dt} = \begin{cases} -\dfrac{N_j P_j}{\tau_\mathrm{a}} \exp\left(\dfrac{l_\mathrm{a}[f_j - f_\mathrm{cri}^\mathrm{m}]}{kT}\right), & \text{if } f_j > f_\mathrm{cri}^\mathrm{m}, \\ 0, & \text{if } f_j \le f_\mathrm{cri}^\mathrm{m}, \end{cases} \tag{18}$$

where τ_a and l_a denote the relaxation time and the activation length for bond dissociation, respectively. The parameter f_j represents the tensile force acting on the polymer chains in the jth network, as defined in Eq. 5. The parameter $f_\mathrm{cri}^\mathrm{m}$ denotes the critical force threshold for damage initiation in molecular chains. According to Eq. 18, damage begins to evolve when the chain force f_j exceeds $f_\mathrm{cri}^\mathrm{m}$, governing both the initiation and progression of damage. Conversely, chains remain intact when $f_j \le f_\mathrm{cri}^\mathrm{m}$.

Furthermore, by introducing the normalized chain force defined in Eq. 6, the damage criterion can be reformulated as

$$\frac{dP_j}{dt} = \begin{cases} -\dfrac{N_j P_j}{\tau_\mathrm{a}} \exp\left(\dfrac{l_\mathrm{a}[\overline{f}_j - \overline{f}_\mathrm{cri}^\mathrm{m}]}{b}\right), & \text{if } \overline{f}_j > \overline{f}_\mathrm{cri}^\mathrm{m}, \\ 0, & \text{if } \overline{f}_j \le \overline{f}_\mathrm{cri}^\mathrm{m}, \end{cases} \tag{19}$$

where $\overline{f}_\mathrm{cri}^\mathrm{m}$ is the normalized critical force for damage, defined as $\overline{f}_\mathrm{cri}^\mathrm{m} = \dfrac{f_\mathrm{cri}^\mathrm{m} b}{kT}$. The detailed numerical implementation can be found in Appendix A. In summary, the initiation of damage is governed by the magnitude of the chain force, while its evolution follows a time-dependent kinetic law.

3.4. Force-dependent chemical reaction of mechanophores

In this subsection, we establish the activation law governing the behavior of mechanophores. Given that mechanophores are covalently incorporated into the first network, our analysis focuses exclusively on the chains within this network. Each subnetwork in the first network exhibits distinct characteristic chain lengths. Rhodamine-based mechanophores

are assumed to be homogeneously distributed within the first network. The number of mechanophores associated with the jth subnetwork is proportional to the volume fraction of the jth subnetwork in the first network (Wang et al. 2015a). Assuming incompressibility for all networks within the elastomer, the volume fraction of the jth subnetwork per unit volume of the elastomer can be expressed as (Wang et al. 2015a)

$$\phi_j = \frac{N_j n_j}{\sum_i N_i n_i}, \quad j = 1, ..., M. \tag{20}$$

According to Eq. 7, ϕ_j can be further represented as

$$\phi_j = \frac{N_j P_{j0}}{\sum_i N_i P_{i0}}. \tag{21}$$

In the Eq. (21), P_{j0} denotes an initial parameter defined in the reference configuration, representing the density of polymer chains with a given characteristic length.

Thus, the number of mechanophores on the jth subnetwork per unit volume of the first network is calculated as

$$c_j = c\phi_j = c\frac{N_j P_{j0}}{\sum_i N_i P_{i0}}, \tag{22}$$

where c denotes the total number of mechanophores per unit volume of the first network. Since the total number of mechanophores remains constant and the elastomer is assumed incompressible, c is invariant throughout the deformation process.

Unactivated mechanophores exhibit blue fluorescence under UV illumination while remain colorless under visible light. Upon reaching a critical force, they undergo force-induced transformation into an activated configuration characterized by salmon pink fluorescence and rose-red coloration. This activated state is thermally reversible, reverting to the unactivated state upon heating or resting. At any given moment, each mechanophore exists in either the unactivated or activated state. In each jth subnetwork, the number of mechanophores are represented by c_j^{U} and c_j^{A}, corresponding to the unactivated and activated states, respectively. Due to the conservation law, they satisfy

$$c_j^{\mathrm{U}} + c_j^{\mathrm{A}} = c_j. \tag{23}$$

According to the theory of reversible reactions (Wang et al. 2015a, Silberstein et al. 2013), we consider the process of

mechanophores switching from unactivated to activated states as the forward reaction, and the transition from activated back to unactivated states as the backward reaction. Let k_j^{f} and k_j^{r} denote the forward and backward reaction rates on the jth subnetwork, respectively. They obey the chemical kinetics equation (Ribas-Arino and Marx 2012, Kauzmann and Eyring 1940), expressed as

$$\frac{dc_j^{\mathrm{A}}}{dt} = k_j^{\mathrm{f}}\, c_j^{\mathrm{U}} - k_j^{\mathrm{r}}\, c_j^{\mathrm{A}}. \tag{24}$$

Since macroscopic chemical response stems from activated mechanophores, our primary focus lies on the number of c_j^{A}. Substituting Eq. 23 into Eq. 24, we obtain a simplified form (Wang et al. 2015a, Silberstein et al. 2013):

$$\frac{dc_j^{\mathrm{A}}}{dt} = k_j^{\mathrm{f}} c_j - [k_j^{\mathrm{f}} + k_j^{\mathrm{r}}] c_j^{\mathrm{A}}. \tag{25}$$

Following the Eyring-Polanyi equation (Eyring and Polanyi 1931), the reaction rate constant k_1, ($k_1 = kT/h\,\exp(-\Delta E/[kT])$, where h is Planck's constant) depends on the activation energy ΔE following an Arrhenius relationship. Transition state theory suggests that the applied force can modify the reaction pathway by reducing the activation barrier for mechanophore conversion. To account for this mechanochemical coupling, we incorporate the influence of molecular chain forces on both reaction kinetics and activation energy. Accordingly, the forward and backward reaction rates for the jth subnetwork in the deformed state are expressed as

$$\begin{aligned} k_j^{\mathrm{f}} &= \frac{kT}{h}\exp\left(-\frac{\Delta E_j^{\mathrm{f}}}{kT}\right), \quad k_0^{\mathrm{f}} = \frac{kT}{h}\exp\left(-\frac{\Delta E_0^{\mathrm{f}}}{kT}\right), \\ k_j^{\mathrm{r}} &= \frac{kT}{h}\exp\left(-\frac{\Delta E_j^{\mathrm{r}}}{kT}\right), \quad k_0^{\mathrm{r}} = \frac{kT}{h}\exp\left(-\frac{\Delta E_0^{\mathrm{r}}}{kT}\right), \end{aligned} \tag{26}$$

where k_0^{f}, k_0^{r}, ΔE_0^{f}, and ΔE_0^{r} correspond to the forward reaction rate, backward reaction rate, activation energies for forward reaction, and backward reaction in the undeformed state, respectively. It is noted that since k_0^{f} and k_0^{r} appear in Eq. 28 below, we give their definitions here for clarity. Besides, k_j^{f} and k_j^{r} are the forward and backward reaction rates on the jth subnetwork under deformation, respectively. The quantities ΔE_j^{f} and ΔE_j^{r} denote activation energies for forward and backward reactions in the deformed state, both of which depend on the applied force.

As shown in Fig. 3, the application of a force on a mechanophore can alter its activation energy. Kim et al. (2016) demonstrated the stress-dependence through using spiropyran-based kinetic probes. Below a critical force level, there is no observable change in reaction kinetics. Once the force exceeds a critical threshold, the forward reaction rate increases while the backward reaction rate decreases with increasing applied force. This behavior arises because the

critical force lowers the activation energy for forward transition, while it raises the barrier for the backward reaction.

Based on these experimental insights, we propose a scheme describing the dependence of microscopic force on activation energies, as shown in Fig. 3. At the molecular scale, when microscopic chain force reaches a critical value, activation energies adopt the following forms:

$$\Delta E_j^{\mathrm{f}} = \begin{cases} \Delta E_0^{\mathrm{f}} - [f_j - f_{\mathrm{cri}}^{\mathrm{c}}]\Delta x^{\mathrm{f}}, & \text{if } f_{\mathrm{cri}}^{\mathrm{c}} < f_j < f_{\mathrm{cri}}^{\mathrm{m}}, \\ \Delta E_0^{\mathrm{f}}, & \text{else}, \end{cases} \tag{27a}$$

$$\Delta E_j^{\mathrm{r}} = \begin{cases} \Delta E_0^{\mathrm{r}} + [f_j - f_{\mathrm{cri}}^{\mathrm{c}}]\Delta x^{\mathrm{r}}, & \text{if } f_{\mathrm{cri}}^{\mathrm{c}} < f_j < f_{\mathrm{cri}}^{\mathrm{m}}, \\ \Delta E_0^{\mathrm{r}}, & \text{else}, \end{cases} \tag{27b}$$

where $f_{\mathrm{cri}}^{\mathrm{c}}$ is the critical force for chemical activation energy change. For ring-opening mechanophores (e.g., rhodamine or spiropyran derivatives), it is well established that $f_{\mathrm{cri}}^{\mathrm{c}} < f_{\mathrm{cri}}^{\mathrm{m}}$, as mechanochemical activation occurs at lower forces than those causing polymer backbone damage. The parameters Δx^{f} and Δx^{r} represent effective distances along the reaction coordinate x from the unactivated state to the transition state, and from the transition state to the activated state, respectively, as depicted in Fig. 3.

When the microscopic force acting on the jth subnetwork exceeds the chemical critical force but remains below the mechanical critical force, the forward activation energy decreases while the backward activation energy increases. This mechanochemical coupling captures the effect of moderate mechanical stimulation, facilitating activation without inducing structural failure. It is conceptually consistent that, when the applied force is below the chemical threshold, mechanophores remain unactivated due to insufficient energy input to overcome the activation barrier. Conversely, when the applied force surpasses the mechanical threshold, activation energies revert to their undeformed values because polymer chains undergo damage behavior governed by Eq. 18. In this regime, most chains within the subnetwork cannot sustain the applied load, leading to chain degradation rather than mechanochemical activation. According to the report of spiropyran-based mechanophores (Silberstein et al. 2013, 2014), Δx^{f} and Δx^{r} should be on the same order (10^{-10} m). For simplicity, we assume $\Delta x^{\mathrm{f}} = \Delta x^{\mathrm{r}} = \Delta x$, followed the treatment proposed by Wang et al. (2015a).

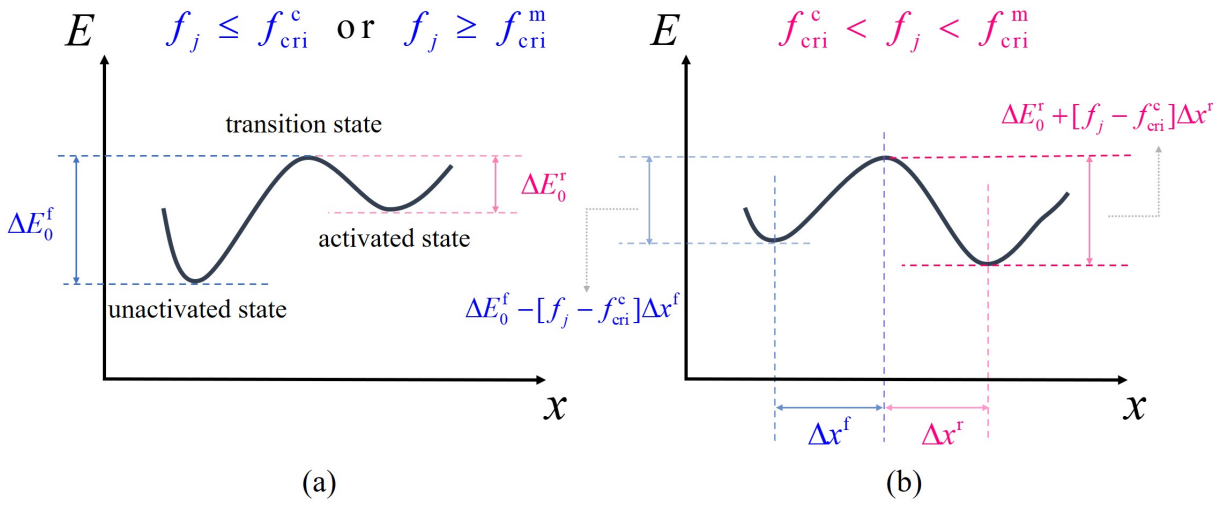

Figure 3: Energy barriers for ring-opening-based mechanophores under different conditions: (a) $f_j \le f_{\mathrm{cri}}^{\mathrm{c}}$ or $f_j \ge f_{\mathrm{cri}}^{\mathrm{m}}$, and (b) $f_{\mathrm{cri}}^{\mathrm{c}} < f_j < f_{\mathrm{cri}}^{\mathrm{m}}$. When the applied chain force falls between two critical values ($f_{\mathrm{cri}}^{\mathrm{c}} < f_j < f_{\mathrm{cri}}^{\mathrm{m}}$), it lowers the activation energy for the forward (ring-opening) reaction while increasing the barrier for the backward reaction. Outside this force range, the energy barriers remain unchanged.

The corresponding evolution of forward and backward reaction rates on the jth subnetwork, k_j^{f} and k_j^{r}, can be represented as

$$k_j^{\mathrm{f}} = \begin{cases} k_0^{\mathrm{f}} \exp\left(\dfrac{[\overline{f}_j - \overline{f}_{\mathrm{cri}}^{\mathrm{c}}]\Delta x}{b}\right), & \text{if } \overline{f}_{\mathrm{cri}}^{\mathrm{c}} < \overline{f}_j < \overline{f}_{\mathrm{cri}}^{\mathrm{m}}, \\ k_0^{\mathrm{f}}, & \text{else}, \end{cases} \tag{28a}$$

$$k_j^{\mathrm{r}} = \begin{cases} k_0^{\mathrm{r}} \exp\left(-\dfrac{[\overline{f}_j - \overline{f}_{\mathrm{cri}}^{\mathrm{c}}]\Delta x}{b}\right), & \text{if } \overline{f}_{\mathrm{cri}}^{\mathrm{c}} < \overline{f}_j < \overline{f}_{\mathrm{cri}}^{\mathrm{m}}, \\ k_0^{\mathrm{r}}, & \text{else}. \end{cases} \tag{28b}$$

Here, $\overline{f}_j$, $\overline{f}_{\mathrm{cri}}^{\mathrm{c}}$, and $\overline{f}_{\mathrm{cri}}^{\mathrm{m}}$ denote normalized chain force on the jth subnetwork, normalized critical force for activation, and normalized critical force for damage, respectively, defined as

$$\overline{f}_j = \frac{f_j b}{kT}, \quad \overline{f}_{\mathrm{cri}}^{\mathrm{c}} = \frac{f_{\mathrm{cri}}^{\mathrm{c}} b}{kT}, \quad \overline{f}_{\mathrm{cri}}^{\mathrm{m}} = \frac{f_{\mathrm{cri}}^{\mathrm{m}} b}{kT}. \tag{29}$$

By substituting Eq. 28 into Eq. 25, the kinetic evolution equation of mechanophores in the jth subnetwork is explicitly

expressed as

$$\frac{d(c_j^{\mathrm{A}}/c)}{dt} = \begin{cases} -\left[k_0^{\mathrm{f}}\exp\left(\dfrac{[\overline{f}_j-\overline{f}_{\mathrm{cri}}^{\mathrm{c}}]\Delta x}{b}\right)+k_0^{\mathrm{r}}\exp\left(-\dfrac{[\overline{f}_j-\overline{f}_{\mathrm{cri}}^{\mathrm{c}}]\Delta x}{b}\right)\right]\dfrac{c_j^{\mathrm{A}}}{c}+k_0^{\mathrm{f}}\exp\left(\dfrac{[\overline{f}_j-\overline{f}_{\mathrm{cri}}^{\mathrm{c}}]\Delta x}{b}\right)\dfrac{N_jP_j}{\sum_i N_iP_i}, \\ \overline{f}_{\mathrm{cri}}^{\mathrm{c}} < \overline{f}_j < \overline{f}_{\mathrm{cri}}^{\mathrm{m}}, \\ \\ -[k_0^{\mathrm{f}}+k_0^{\mathrm{r}}]\dfrac{c_j^{\mathrm{A}}}{c}+k_0^{\mathrm{f}}\dfrac{N_jP_j}{\sum_i N_iP_i}, \quad \text{else}, \end{cases} \tag{30}$$

where c_j^{A}/c represents the fraction of activated mechanophores in the jth subnetwork relative to the total mechanophore content in the first network. Eq. 30 is a first-order ordinary differential equation for c_j^{A}/c, solvable via standard numerical methods. Based on the computed concentrations of activated mechanophores in each subnetwork, the total concentration of activated mechanophores in the first network (c^{A}/c) can be expressed as

$$\frac{c^{\mathrm{A}}}{c} = \sum_j \frac{c_j^{\mathrm{A}}}{c}. \tag{31}$$

Having established the microscopic dynamic evolution of mechanophore activation, we now relate the microscopic population of activated mechanophores to macroscopic optical signals. Following established methodologies, it is assumed that the macroscopic fluorescence intensity of elastomers scales proportionally with the total activated mechanophore concentration across the entire elastomer (Sun et al. 2024). Accordingly, the observed fluorescence intensity Q can be represented as

$$Q = k_0\frac{c^{\mathrm{A}}}{c}, \tag{32}$$

where k_0 is a proportionality constant. It should be noted that, unlike in the previous work by Wang et al. (2015a), Eq. 32 in our model does not require explicit thickness correction. This distinction arises because our experimental fluorescence signals have been pre-corrected for thickness variations in the deformed state. In contrast, Wang et al. (2015a) measured fluorescence intensity per unit area, necessitating thickness correction in their formulation.

The term chemo-mechanical used in this work refers to a one-way coupled framework, in which the chemical process, namely the activation of mechanophores, is driven by the mechanical response. When the chain force reaches the critical activation threshold $\overline{f}_{\mathrm{cri}}^{\mathrm{c}}$, force-induced ring-opening reactions are triggered. When the force further exceeds the critical damage threshold $\overline{f}_{\mathrm{cri}}^{\mathrm{m}}$, chain damage promotes ring-closing reactions, rendering the mechanophores irreversibly inactive. In contrast, the mechanical constitutive behavior itself is not affected by the chemical reactions.

In the model, the externally applied deformation is first transmitted to the molecular scale, and the force carried by individual polymer chains is described by Eq. (6). This chain-level force subsequently drives the activation of mechanophores, whose evolution is governed by Eq. (30). In this manner, the chemical reaction process is coupled to the mechanical response through the microscopic chain force. Owing to the one-way nature of the coupling, the parameters associated with the chemical reaction do not enter the mechanical constitutive relations and therefore do not influence the macroscopic stress–strain response.

4. Parametric study

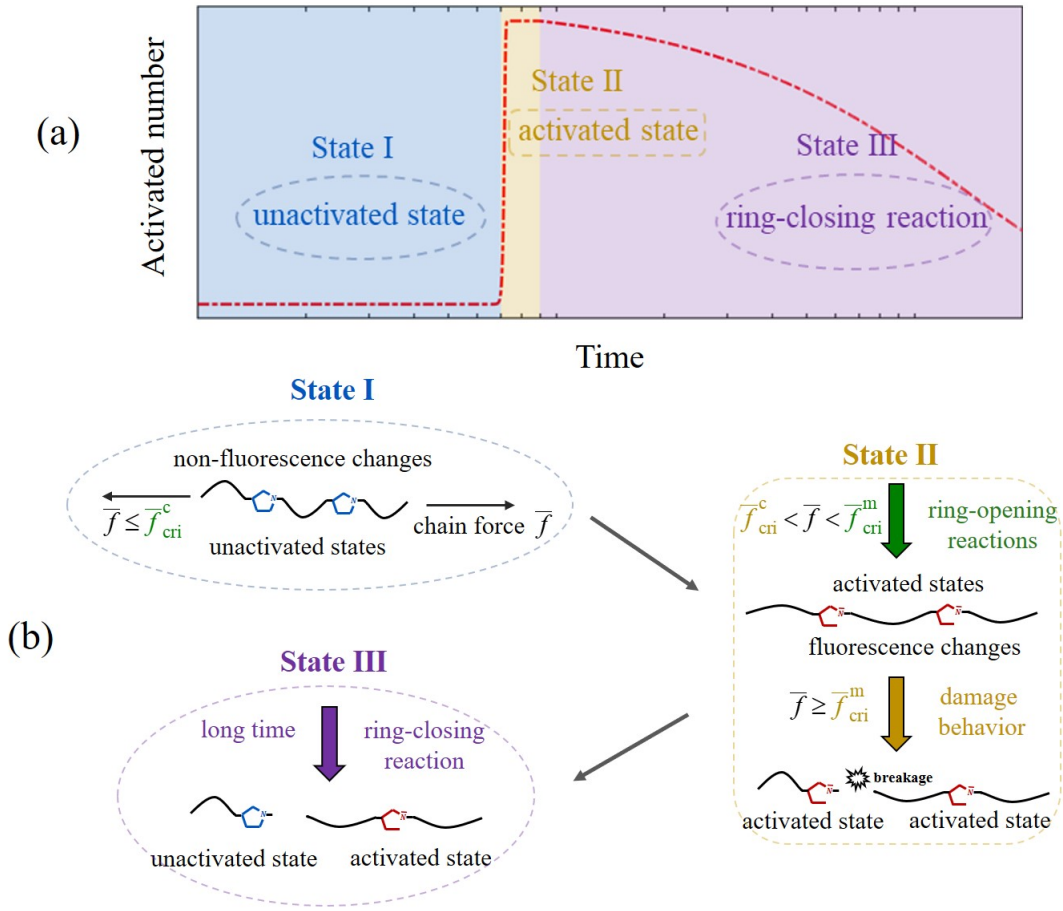

Figure 4: (a) The number of activated mechanophores as a function of time for a single type of polymer chain under applied force. (b) Schematic illustration for the evolutions of mechanochemical activation and damage under three distinct states. State I: The applied stress remains below the activation threshold of the mechanophores ($\overline{f} \le \overline{f}^{c}_{cri}$), resulting in no fluorescence emission; State II: Mechanophores start to emit fluorescence and chain damage occurs ($\overline{f} > \overline{f}^{c}_{cri}$); State III: Mechanophores on damaged chains gradually return to their non-fluorescent state.

We begin by examining the ring-opening and ring-closing dynamics of mechanophores and the associated damage behavior in a single polymer chain under applied force. As illustrated in Fig. 4, the mechanochemical behavior can be classified into three distinct regimes:

State I: When the chain force remains below the chemical critical threshold $\overline{f} \leq \overline{f}^{\mathrm{c}}_{\mathrm{cri}}$, mechanophores remain inactive, exhibiting no fluorescence changes.

State II: Upon exceeding the chemical critical force $\overline{f} > \overline{f}^{\mathrm{c}}_{\mathrm{cri}}$, mechanophore activation occurs. This state features two sub-regimes:

-For $\overline{f}^{\mathrm{c}}_{\mathrm{cri}} < \overline{f} < \overline{f}^{\mathrm{m}}_{\mathrm{cri}}$, the forward reaction rate increases, promoting mechanophore activation through ring-opening.

-For $\overline{f}^{\mathrm{m}}_{\mathrm{cri}} \leq \overline{f}$, chain fracture initiates, drastically reducing force-bearing capacity and consequently decreasing the forward reaction rate. Notably, activated mechanophores do not immediately revert to their ground state. Given the slow backward reaction rate ($k^{\mathrm{r}}_0 \sim 10^{-5}$ to 10^{-4} /s), elastically inactive mechanophores associated with broken chains require substantial time to complete ring-closing.

State III: During this phase, elastically inactive mechanophores gradually return to their non-fluorescent state via ring-closing reactions, while intact mechanophores remain unaffected.

4.1. Number of segments

We now systematically examine how the mechanochemical response is influenced by various model parameters for single-chain networks in TN elastomers under uniaxial tension. We assume the initial chain density of the single type chains is 1, i.e., P = 1. The other benchmark parameters are listed in Tab. 2 if not otherwise specified. First, we consider chains with different segment numbers ($N = 6.0, 6.5, 7.0$, and 8.0) elongated to a stretch ratio of 2.5 at a stretch rate of 0.01 /s. The predicted response is shown in Fig. 5. The single-chain force-stretch curves (Fig. 5-(a)) reveal that the strain stiffening effect initiates later with increasing N. Shorter chains exhibit earlier damage onset (Fig. 5-(b)), consistent with our established damage criterion. The mechanochemical response is characterized by plotting the normalized concentration of activated mechanophores (c^{A}/c) versus stretch ratio, and normalized chain force (Fig. 5 (c)-(d)). It shows that longer chains require larger stretch to activate because of the delayed strain stiffening effect. As shown, although the chain is broken and the chain density value approximately decreases to zero under large deformation (Fig. 5-(b)), the predicted value of c^{A}/c (Fig. 5-(c)) shows only gradual decay rather than immediate disappearance, because the elastically inactive mechanophores need time to become non-fluorescent. As can be seen from Fig. 5-(d), all the curves overlap and the critical force for activation is about 580 for all different chains. It illustrates that the mechanophores on different-length chains obey the same activation criteria. However, it is noted that the model parameter $\overline{f}^{\mathrm{c}}_{\mathrm{cri}}$ of normalized critical force for activation was set as 500. The discrepancy

between the preset value and the simulated value is due to the time-dependent nature of the mechanophore activation. As a consequence, a discussion of the influence of stretch rate is included as follows.

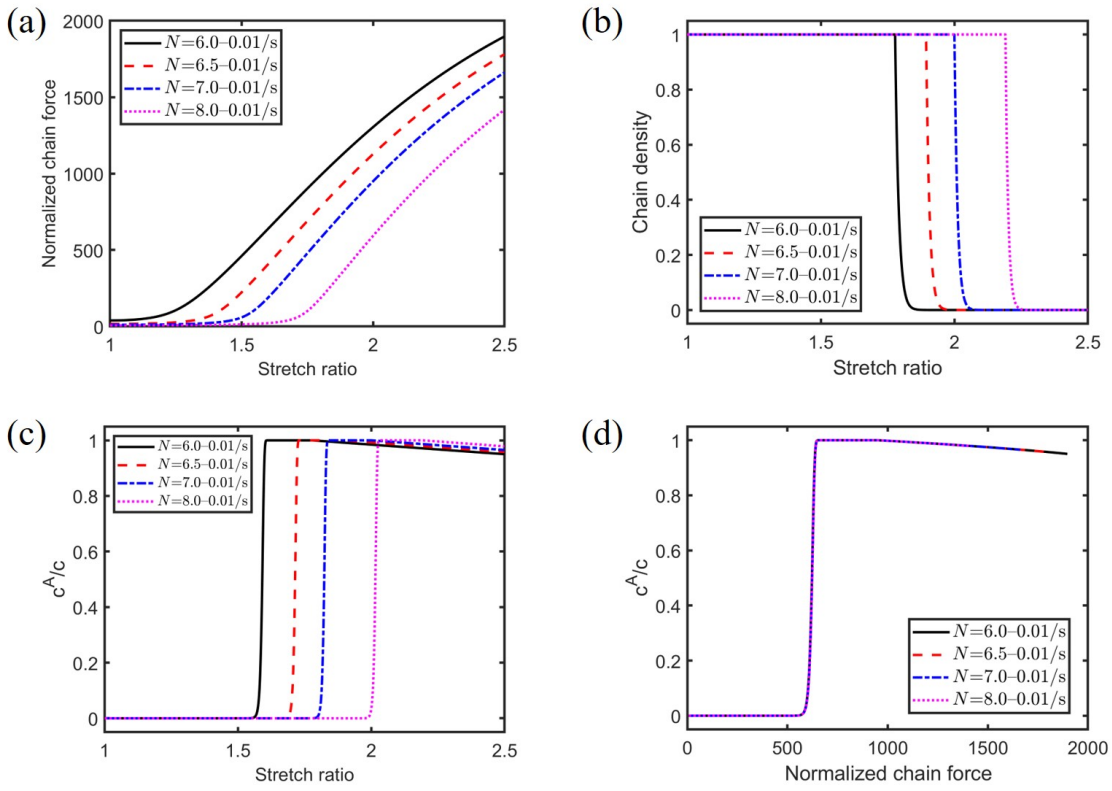

Figure 5: Influence of polymer chain segment number on response: (a) normalized chain force ($\overline{f}$), (b) chain density (P), (c) normalized concentration of activated mechanophores (c^{A}/c), as a function of the stretch ratio, and (d) c^{A}/c as a function of $\overline{f}$. The simulations were conducted at a loading rate of 0.01 /s up to a maximum stretch of 2.5.

4.2. Loading stretch rates

To investigate the effect of stretch rate, the single chains ($N = 6.0$) are elongated to a stretch ratio of 2.0 at different stretch rates of 0.01/s, 0.001/s, 0.0001/s, and 0.00001/s, respectively. All force-stretch curves at different rates overlap (Fig. 6-(a)). Since the damage criterion constructed in the last section is rate-dependent, it is reasonable that chain density under lower rate conditions approach zero under smaller deformations (Fig. 6-(b)). To understand the mechanochemical behavior, we plot the c^{A}/c as functions of time, and normalized chain force as shown in Figs. 6 (c)-(d).

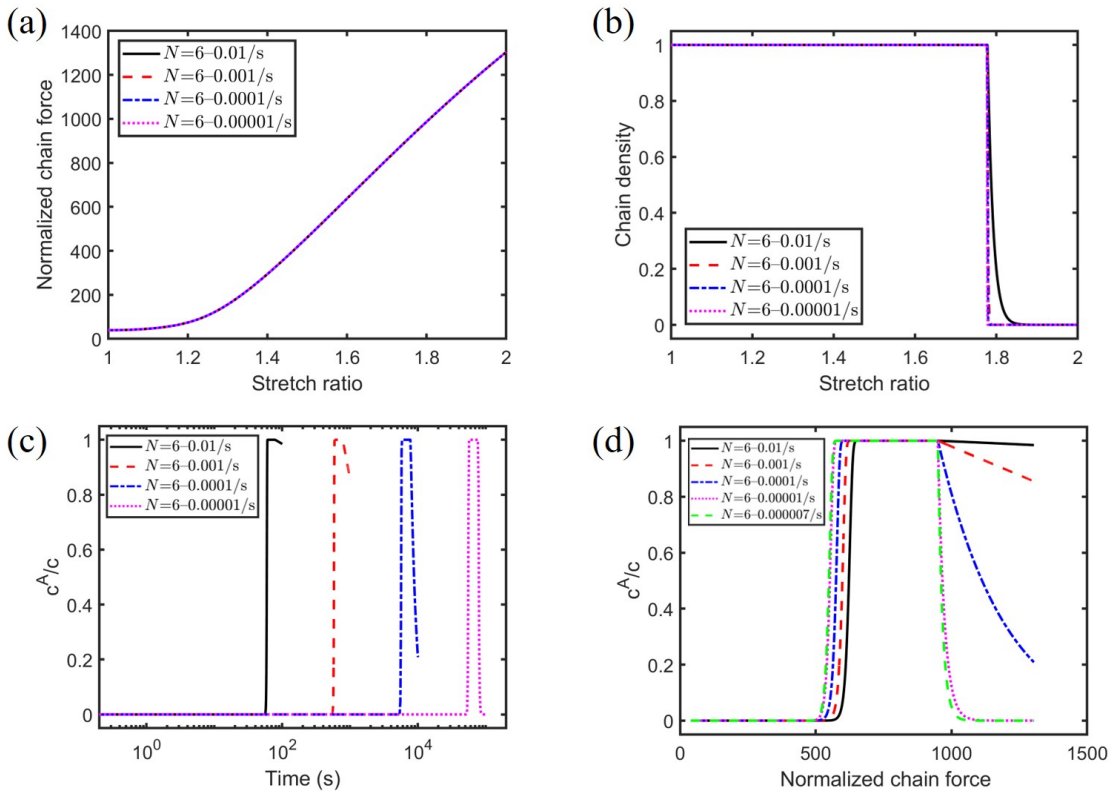

Figure 6: Influence of loading rates on response: (a) normalized chain force ($\overline{f}$), (b) chain density (P) as functions of stretch ratio; (c) normalized concentration of activated mechanophores (c^{A}/c) as a function of time, and (d) c^{A}/c as a function of $\overline{f}$. Panel (d) includes an additional ultra-slow loading case (0.000007 /s). Simulations were performed at a maximum stretch of 2.0 for polymer chains with segment number $N = 6$.

A shorter activation time of mechanophores is observed at higher stretch rates. When the chain suffers damage, these activated mechanophores start to return to ring-closing structure. It can be seen from Fig. 6-(c) that a lower stretch rate makes more elastically inactive mechanophores revert to unactivated states. This is because a lower rate allows more time for ring-closing reactions to occur. Furthermore, the ring-closing reaction is closely related to the model parameter of forward reaction rate k_0^{f}, which is discussed in the following subsection. As demonstrated from Fig. 6-(d), a decreased stretch rate results in a lower critical activated force. In particular, the simulated critical force for activation at the rate of 10^{-5} /s is approximately 500, which is equal to the preset model parameter $\overline{f}_{\mathrm{cri}}^{\mathrm{c}} = 500$. It can also explain the discrepancy between the preset value $\overline{f}_{\mathrm{cri}}^{\mathrm{c}}$ and the simulated value at a larger rate of 0.01 /s in the last subsection. Additionally, a simulation at a stretch rate of $7 * 10^{-6}$ /s is included in Fig. 6-(d). The response for the loading rates of 10^{-5} /s and $7 * 10^{-6}$ /s is consistent. It indicates that when the timescale of the loading rate is close to the timescale of preset forward reaction rate $k_0^{\mathrm{f}} = 7 * 10^{-6}$ /s, the simulated critical force for activation is consistent with the preset value.

4.3. Normalized critical force for activation

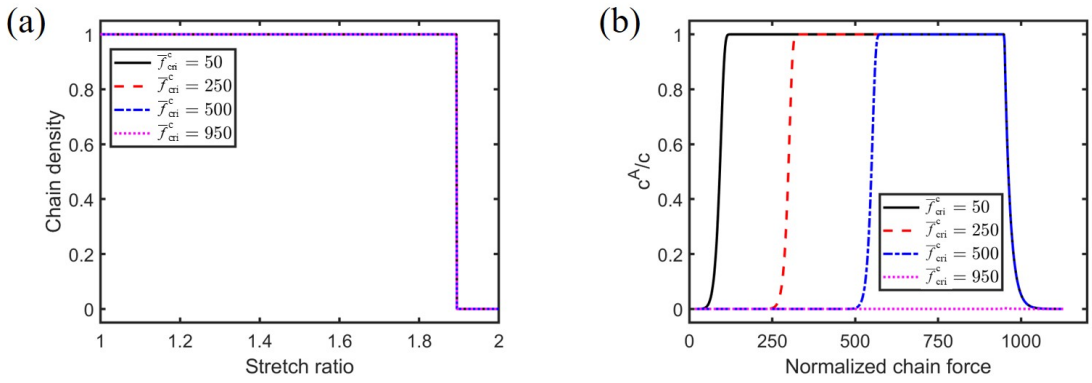

Figure 7: Influence of normalized critical force for activation ($\overline{f}^{c}_{cri}$) on the response of (a) chain density (P) as a function of stretch ratio and (b) normalized concentration of activated mechanophores (c^A/c) as a function of normalized chain force ($\overline{f}$). Simulations were performed under quasi-static loading (rate: $7{*}10^{-6}$ /s) with a maximum applied stretch of 2.0.

In this subsection, the single chains ($N = 6.5$) are elongated to a stretch ratio of 2.0 at a low stretch rate of $7 * 10^{-6}$ /s with different values of normalized critical force for activation ($\overline{f}^{c}_{cri} = 50, 250, 500, 950$). As shown in Fig. 7-(a), the resulting chain density–stretch curves overlap throughout the entire simulation. This is because the model parameters related with chemical reactions such as $\overline{f}^{c}_{cri}$, k^{r}_{0}, k^{f}_{0}, do not influence the damage law (Eq. 6) whereas parameters related with mechanical parts can affect the mechanochemical behavior. To exhibit mechanochemical response, the total concentration of activated mechanophores c^A/c as a function of normalized chain force is plotted in Fig. 7-(b). In the case of $\overline{f}^{c}_{cri} < \overline{f}^{m}_{cri} = 950$, a larger value of $\overline{f}^{c}_{cri}$ causes a larger critical normalized chain force required to trigger activation. However, when the preset value of $\overline{f}^{c}_{cri} \geq \overline{f}^{m}_{cri}$ (though in the present mechanophore system, this case does not occur), the chains undergo damage before occurrence of any ring-opening reactions, thereby preventing fluorescence activation. Besides, since the simulated stretch rate is small enough, all the elastically inactive mechanophores have adequate time to revert to unactivated states.

4.4. Forward and backward reaction rates

In the previous subsection, it was observed that all the aforementioned model parameters influence the forward reactions of mechanophores. It is reasonable to infer that the parameter governing the forward reaction rate, k^{f}_{0}, also plays a significant role. Thus, the effect of parameter k^{f}_{0} is presented in Fig. 8. We plot the c^A/c as a function of stretch ratio and normalized chain force, which show lower critical stretch ratios and chain forces required for activation with

increasing the value of k_0^{f}. Interestingly, despite sharing the same backward reaction rate (i.e., $7*10^{-4}$ /s), their ring-closing response is different. Specifically, the c^{A}/c with a forward reaction rate parameter $k_0^{\mathrm{f}} = 7*10^{-2}$ /s exhibits the most dramatic decrease, while other cases show only minor reductions. According to Eq. 30, the evolution of the ring-closing reaction is associated with the parameter $k_0^{\mathrm{f}} + k_0^{\mathrm{r}}$. It implies that when $k_0^{\mathrm{r}} \gg k_0^{\mathrm{f}}$, the value of k_0^{r} becomes dominant. Thus, the decreased curves with $k_0^{\mathrm{f}} = 7*10^{-6}$ /s and $k_0^{\mathrm{f}} = 7*10^{-8}$ /s overlap. In contrast, when the value of k_0^{f} is sufficiently large ($7*10^{-2}$ /s), it becomes the dominant factor, accelerating the ring-closing reaction and leading to a rapid decline in the concentration of activated mechanophores. It is worth noting that, in practice, the backward reaction rate under a no force condition is typically much larger than the forward reaction rate (i.e., $k_0^{\mathrm{r}} \gg k_0^{\mathrm{f}}$).

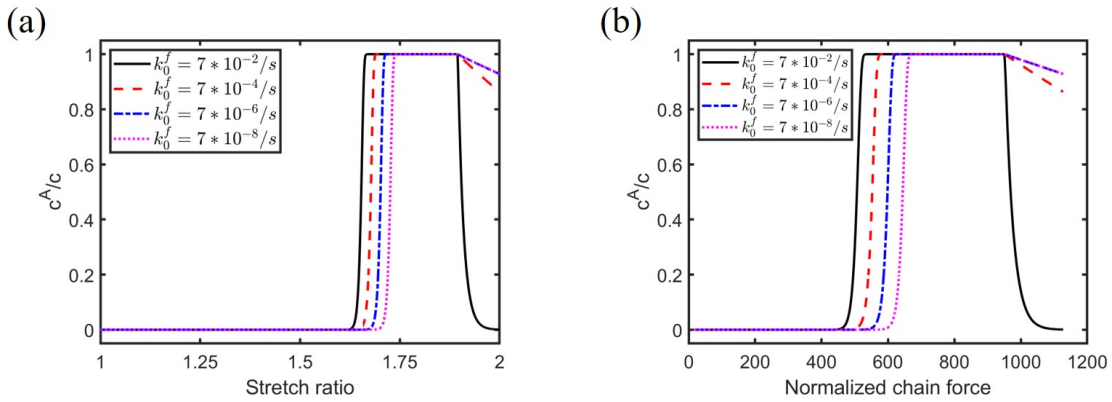

Figure 8: Effect of forward reaction rate (k_0^{f}) on response: (a) normalized concentration of activated mechanophores (c^{A}/c) as a function of stretch ratio and (b) c^{A}/c as a function of the normalized chain force ($\overline{f}$). Simulations were performed at a maximum applied stretch of 2.0 for segment number $N = 6.5$ with a constant loading rate of 0.01 /s.

As previously discussed, the mechanochemical response exhibits dependence on model parameters across different time scales. Thus, the backward reaction rate is also an important factor. The related mechanochemical response is shown in Fig. 9. It shows that different values of the backward reaction rate k_0^{r} lead to consistent critical stretch ratio and normalized chain force for activation. This is because the forward reaction rate is always dominant when the chain force lies between two critical forces, i.e., $\overline{f}_{\mathrm{cri}}^{\mathrm{c}} < \overline{f} < \overline{f}_{\mathrm{cri}}^{\mathrm{m}}$, according to the Eq. 28. In the damage zone, a higher backward reaction rate accelerates the decline in activated mechanophore concentration, which is expected under the condition $k_0^{\mathrm{r}} > k_0^{\mathrm{f}}$.

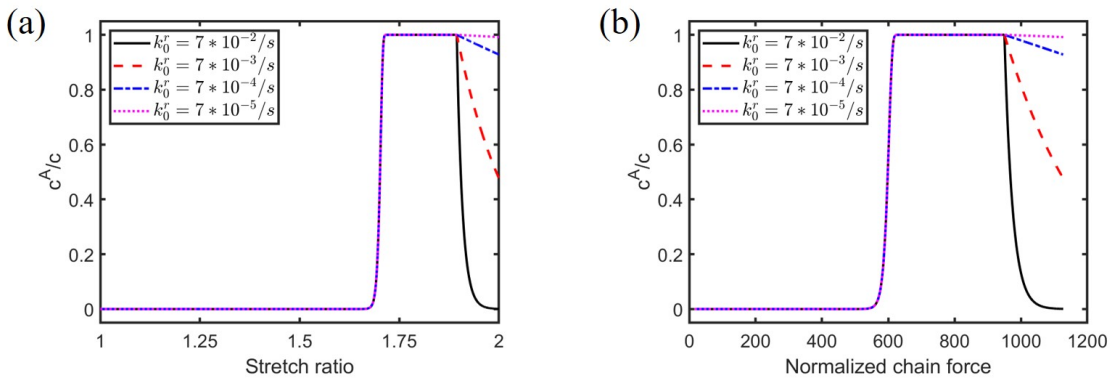

Figure 9: Influence of backward reaction rate (k_0^r) on mechanochemical response: (a) normalized concentration of activated mechanophores (c^{A}/c) as a function of stretch ratio and (b) c^{A}/c as a function of normalized chain force ($\overline{f}$). Simulations were performed at a maximum applied stretch of 2.0 for segment number $N = 6.5$ with a constant loading rate of 0.01 /s.

5. Parameter determination

This section illustrates the calibration of the presented mechanochemical–damage model using experimental data obtained from mechanofluorescent multiple network elastomers. We begin by outlining the parameter determination procedure. For the mechanical part, the shear modulus of the first network G_{f} can be calculated from the small deformation zone of the uniaxial strain-stress curve for the single network (first network) elastomer, which is 0.22 MPa. Additionally, specification of the first-network chain-length distribution is required. We employ the density function introduced by Govindjee and Simo (1991), which has been successfully applied to characterize first network distributions in similar systems (Xiao et al. 2021). The distribution is given by

$$g(x) = \sqrt{\frac{3\kappa^2}{2\pi x}} \exp\left(-G - \frac{\kappa}{\sqrt{\pi}}[\sqrt{6x}\,\mathrm{e}^{-G} + 3\bar{r}\sqrt{\pi}\,\mathrm{erf}(\sqrt{G}) - \sqrt{6}\,\mathrm{e}^{-Gx} - 3\bar{r}\sqrt{\pi}\,\mathrm{erf}(\sqrt{Gx})]\right), \tag{33}$$

where $G = 3\bar{r}^2/[2x]$, $\bar{r}$ denotes the relative distance, and κ is a dispersion parameter. The normalized chain density corresponding to chains with N_j segments is then defined as

$$P_j = \frac{g(N_j)\Delta N}{\sum g(N_j)\Delta N}. \tag{34}$$

The parameters $\bar{r}$, κ, and $\overline{E}$ have a strong effect on stress level, which are calibrated by the uniaxial tension data of SN elastomers. To assess the accuracy of this discretization, we performed a convergence study by comparing the uniaxial

stress–stretch responses obtained with different values of ΔN, as shown in Fig. 10-(a). When a relatively large value of $\Delta N = 0.5$ is used, numerical fluctuations and loss of smoothness are observed, indicating insufficient resolution. In contrast, the responses obtained with $\Delta N = 0.1$ and $\Delta N = 0.05$ are essentially indistinguishable, demonstrating that the discretization is sufficiently fine and that the results have converged. In the present work, a discretization step of $\Delta N = 0.1$ is used over the range $N = 0$–50, resulting in 500 subnetworks as shown in Fig. 10-(b). We note that the specific functional form adopted here serves as a convenient continuous representation for discretization and is not unique. Alternative distributions, such as Gaussian-type chain-length distributions, could also be employed within the same framework without altering the underlying modeling strategy.

The parameters N_{m} and n_{m} are introduced to characterize the mechanical response of the matrix network in the absence of chain damage. This network does not participate in the mechanochemical reactions and primarily serves as a mechanically stable substrate. Owing to its much lower crosslinking density compared to the first network, the matrix network exhibits a smaller shear modulus and a significantly larger characteristic chain length. It is found that, prior to necking, the contribution of the matrix network to the overall stress response is substantially smaller than that of the first network. As a result, the mechanical response and the mechanochemical behavior of interest in the present study are only weakly sensitive to the specific values of N_{m} and n_{m}. Accordingly, the shear modulus of the matrix network is set to $G_{\mathrm{m}} = n_{\mathrm{m}}kT = 0.1$ MPa, which is smaller than G_{f}, and the chain length parameter is chosen as $N_{\mathrm{m}} = 200$, consistent with our previous work (Xiao et al. 2021). This choice reduces the number of fitting parameters in the present model without affecting the main conclusions. The parameters ($\overline{f}^{\mathrm{m}}_{\mathrm{cri}}$, b, τ_a, l_{a}) associated with damage behavior are determined by fitting the cyclic data of TN elastomer.

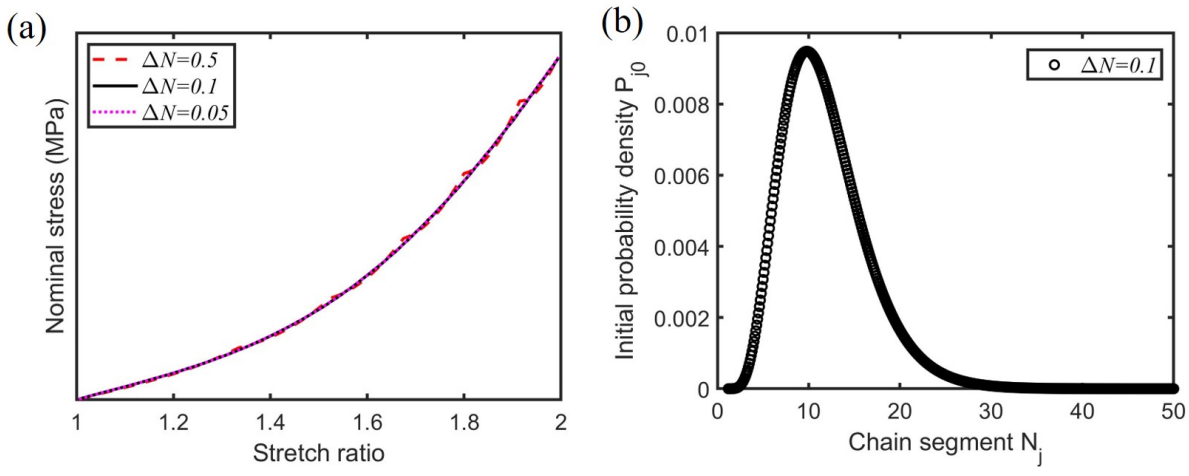

Figure 10: (a) Comparison of predicted uniaxial stress response with different $\Delta N = 0.5, 0.1, 0.05$ and (b) the distribution of chain lengths of the first network with the parameter $\Delta N = 0.1$ (500 subnetworks).

For the chemical part, the backward reaction rate k_0^{r} is identified by fitting the ring-closing evolution of mechanophores under a force-free condition as shown in Fig. 11. The fitting function is a typical relaxation function, which is expressed as $\varphi(t) = \exp(-t/\tau_0)$, where τ_0 is a characteristic time. The value of τ_0 is determined to be 1504 s for sample 1 and 1367 s for sample 2, giving a value of the backward reaction rate $k_0^{\mathrm{r}} = 1/\tau_0 \approx 7 * 10^{-4}$ /s, which is consistent between the two measurements. As discussed in the previous section, the forward reaction rate k_0^{f} under a force-free condition is typically much smaller than the backward reaction rate. Thus, the value of k_0^{f} is set to $7 * 10^{-6}$ /s, two orders of magnitude lower than k_0^{r} (Wang et al. 2015a). The parameter of Δx is set to $1 * 10^{-10}$ m, consistent with reported values for spiropyran mechanophores undergoing ring-opening reactions (Wang et al. 2015a). The remaining parameters ($\overline{f}_{\mathrm{cri}}^{\mathrm{c}}$, k_0) are directly calibrated against fluorescence data of the TN elastomer under loading and reloading tests. The normalized critical activation force, denoted as $\overline{f}_{\mathrm{cri}}^{\mathrm{c}}$, is assigned a value of 500. Utilizing the normalization relationship presented in Eq. 29, the corresponding chain activation force $f_{\mathrm{cri}}^{\mathrm{c}}$ is determined to be 2.1 nN. This value agrees well with the ring-opening forces reported for similar mechanophores (Klein et al. 2020). Table 2 summarizes all model parameters together with their assigned values and physical interpretations.

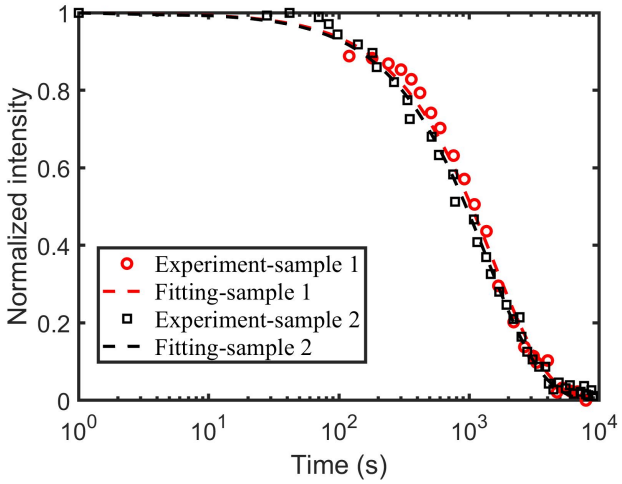

Figure 11: Fitting the experimental intensity response of the ring-closing evolution of mechanophores under the force-free condition.

Table 2: Parameters of the constitutive model.

Parameter	Value	Physical significance
G_{f} in MPa	0.22	Shear modulus of the first network
$\bar{r}$	3.6	Relative distance
κ	5	Dispersion parameter
$\overline{E}$	7000	Normalized bond energy
G_{m} in MPa	0.1	Shear modulus of the matrix
N_{m}	200	Chain length of the matrix
$\overline{f}_{\mathrm{cri}}^{\mathrm{m}}$	950	Normalized critical force for damage
b in m	$1 * 10^{-9}$	Kuhn length
τ_{a} in s	8	Relaxation time for bond dissociation
l_{a} in m	$1.05 * 10^{-12}$	Activation length for bond dissociation
k_0^{f} in s^{-1}	$7 * 10^{-6}$	Forward reaction rate
k_0^{r} in s^{-1}	$7 * 10^{-4}$	backward reaction rate
Δx in m	$1 * 10^{-10}$	Effective distance
$\overline{f}_{\mathrm{cri}}^{\mathrm{c}}$	500	Normalized critical force for activation
k_0	470	Proportional constant

6. Results and discussion

In this section, we apply the model to simulate the response of mechanofluorescent multiple network elastomers. Figs. 12-14 compare the simulation and experimental results of mechanical and fluorescent response for SN, DN, and TN elastomers, respectively. It is clear that the predicted uniaxial stress–strain curve for SN elastomer matches well with the experimental result at a loading rate of 0.05 /s. As expected, neither simulations nor experiments exhibit fluorescence changes in SN elastomers due to stress levels being too low to activate mechanophores.

For the mechanical response of DN elastomers at a loading rate of 0.05 /s, the model describes the cyclic behavior reasonably well, though it slightly underestimates the stress level under moderate deformation. As shown in Fig. 13-(b), the model accurately captures the fluorescence response. The predictions show good agreement with experimental

data across two loading cycles. Furthermore, the model successfully reproduces features such as delayed activation and reduced fluorescence intensity in the second cycle, which are attributed to damage accumulated during the first loading cycle.

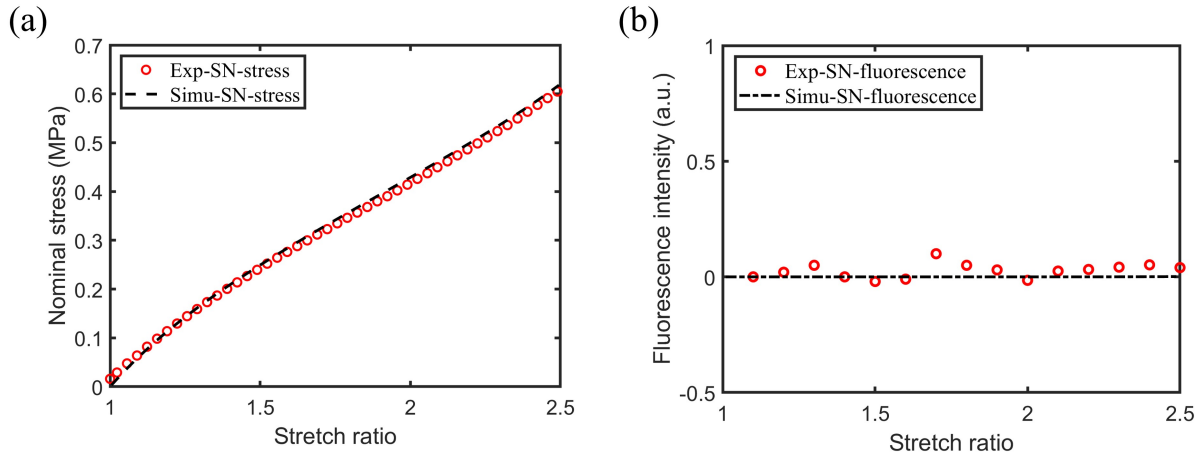

Figure 12: Comparison between the measured and predicted response for SN elastomers under uniaxial loading condition: (a) the stress response and (b) the fluorescence response.

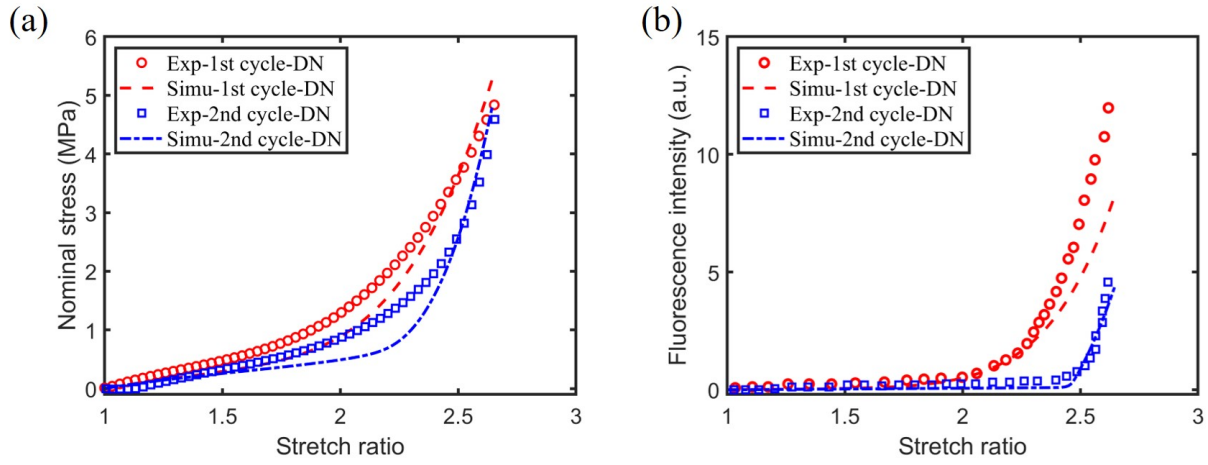

Figure 13: Comparison between the measured and predicted response for DN elastomers in the cyclic loading condition: (a) the stress response and (b) the fluorescence response.

Fig. 14 presents the comparison between simulations and experiments for TN elastomers in loading and reloading tests at strain rates of 0.05 /s and 0.001 /s. The predicted stress response at different strain rates is consistent with experimental results across two loading cycles. The model captures subtle rate-dependent effects because damage evolution is time-dependent (Eq. 18). The damage degree at a higher loading rate is smaller under the same deformation, leading

to slightly larger stress levels at large deformations. Moreover, with increasing deformation, the discrepancy in stress values between the two loading rates increases, which is consistent in both predictions and experiments.

Regarding the mechanochemical response, the predicted fluorescence intensities under different loading rates are generally consistent with the experimentally measured data. Since the simulated stress under small deformation is slightly higher than the experimental stress, the predicted fluorescence is correspondingly larger. These discrepancies are caused by the final drying process during synthesis. Several shorter chains have been ruptured while this effect has been emitted since the prestretch ratio is determined between the dimension of the dry specimen of DN elastomers and the dry state of the corresponding SN elastomers. Furthermore, as discussed in Section 4, a lower strain rate provides more time for mechanophores to fully activate. Therefore, a lower loading rate exhibits a larger fluorescence intensity in simulations. Notably, the difference in simulated fluorescence between the two loading rates decreases during the large deformation stage of the first loading cycle. This is because mechanophores linked to damaged chains have sufficient time to revert to the unactivated state at the lower strain rate of 0.001 /s. The absence of a similar phenomenon in the second loading cycle is due to the limited damage response. All these features are consistently observed in experiments. As discussed in Section 4, mechanochemical response is a complex behavior influenced by both loading rate and damage evolution. Overall, multiple network elastomers exhibit stronger mechanical and fluorescence response with the increase in network number, all of which can be fully captured by the model. More importantly, the model demonstrates the coupled relationship between damage behavior and fluorescence response, consistent with experimental findings. It should be noted that there are several limitations of the present constitutive framework. Specifically, for DN elastomers, the predicted stresses are consistently lower than the experimental measurements, and the fluorescence intensity at maximum stretch in the first loading cycle is not fully captured. In addition, while the model qualitatively reproduces the rate-dependent trends, it does not capture the threshold-like behavior observed in the fluorescence response.

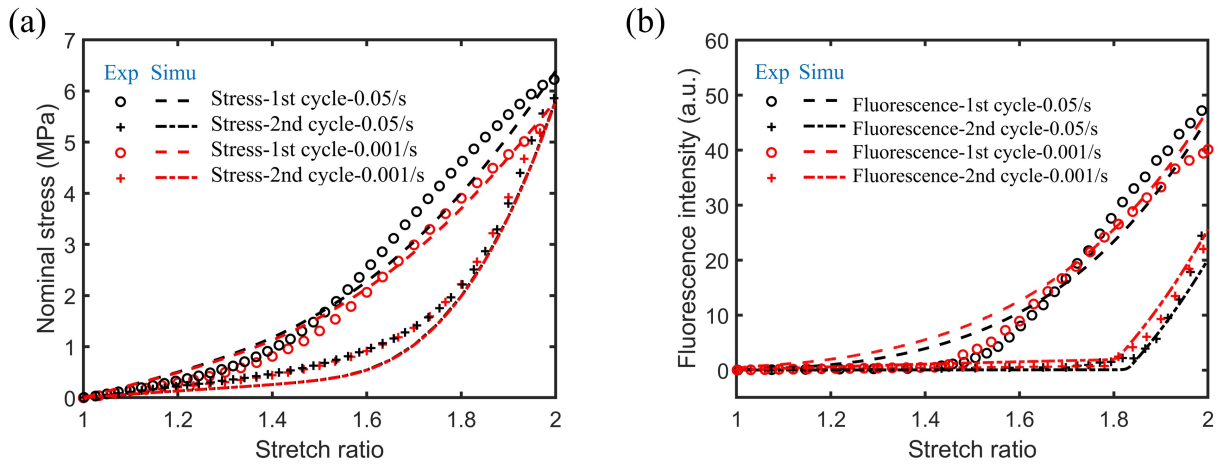

Figure 14: Comparison between the measured and predicted response for TN elastomers in the cyclic loading condition: (a) the stress response and (b) the fluorescence response.

To further evaluate its performance, the proposed model is extended to inhomogeneous deformation conditions. Cyclic uniaxial tension tests were conducted on TN elastomer specimens with defects: one with a pre-punched circular hole (diameter 1 mm) and the other with a pre-cut edge crack (length 1 mm). Simultaneous mechanofluorescent imaging was employed to capture spatial distributions during loading. The effective geometries of the clamping regions for both specimen types are illustrated in Fig. 15.

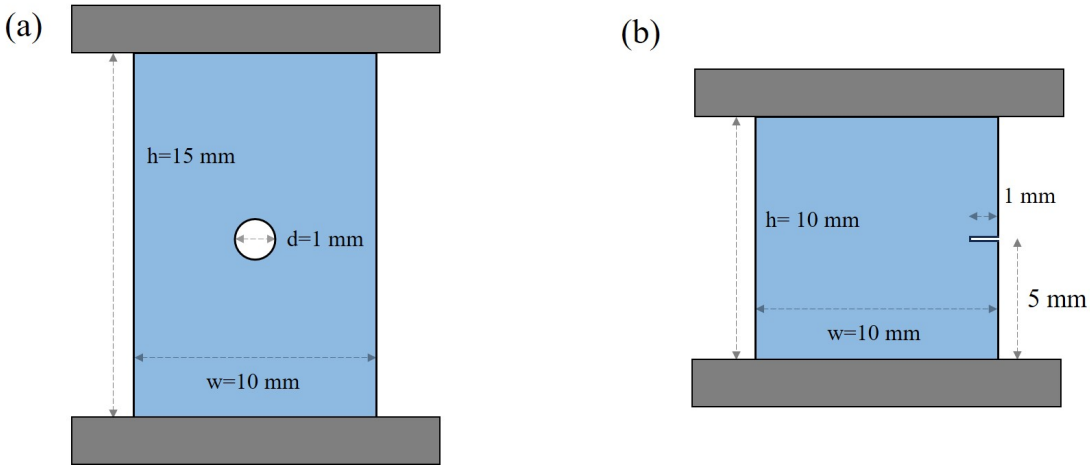

Figure 15: Geometry of the TN elastomer specimen: (a) the sample with a pre-punched circular hole (height: 15 mm, width: 10 mm, hole diameter: 1 mm); (b) the sample with a pre-cut edge crack (height: 10 mm, width: 10 mm, crack length: 1 mm).

The experimental procedure consists of two steps. First, specimens were stretched to a prescribed stretch ratio of 2.0

(or 2.35) at a loading speed of 45 mm/min (or 30 mm/min). Subsequently, following unloading and fluorescence fading treatments, the specimens were reloaded to the same stretch level in the second cycle. We present the displacement-time curves for the pre-holed and pre-cracked TN samples, as shown in Fig. 16-(a) and (b), respectively. For numerical simulations, the previously proposed constitutive model was implemented in COMSOL Multiphysics. The total free energy form is input via the hyperelastic user-defined option under the Solid Mechanics module. The damage criterion for polymer chains and the activation criterion for mechanophores are implemented as the state variables with the details shown in Appendix A.

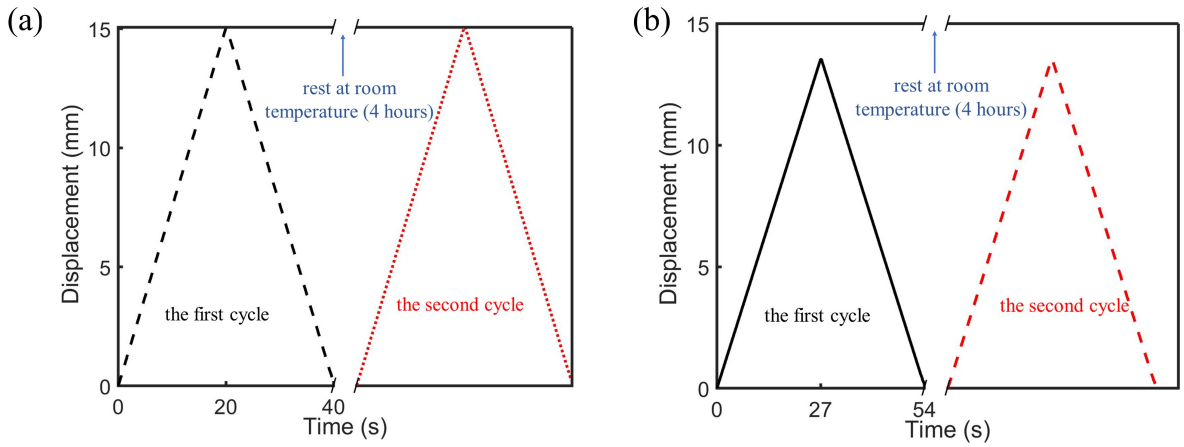

Figure 16: Displacement–time response during cyclic loading and unloading tests for (a) a pre-holed TN elastomer at a loading speed of 45 mm/min and (b) a pre-cracked TN elastomer at a loading speed of 30 mm/min.

Under two-dimensional plane stress conditions, the specimen geometry and boundary constraints exhibit sufficient symmetry. Therefore, computational efficiency is achieved through model reduction. Specifically, only a quarter-domain of the specimen is modeled for the pre-holed configuration and a half-domain for the pre-cracked configuration. The detailed geometric setup and boundary conditions applied in the simulations are provided in Fig. 17. Quadrilateral elements with mesh refinement near the hole or crack are used, as shown in Fig. 17. Post-processing involves mirror reconstruction of the quarter or half models to generate full-field visualizations of the deformed shape and the associated mechanofluorescent response across the entire specimen.

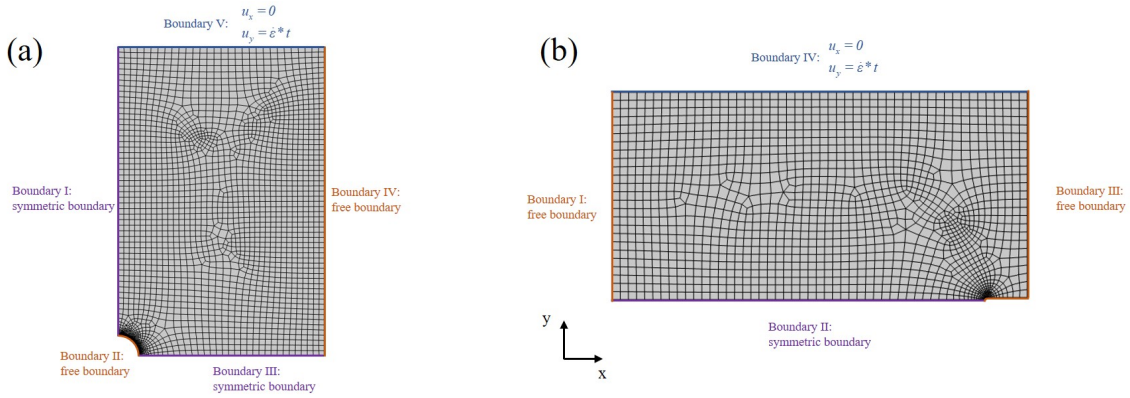

Figure 17: The setup of finite element analysis for (a) the quarter-symmetry model and (b) the half-symmetry model.

We first compare the experimentally measured and simulated force-displacement curves for pre-holed and pre-cracked TN elastomers, as shown in Fig. 18-(a) and (b), respectively, which show general consistency. However, the predictions overestimate the force level especially for pre-cracked specimens in the large deformation region. This discrepancy is possibly caused by the inaccuracy of the distribution of chain lengths for long chains.

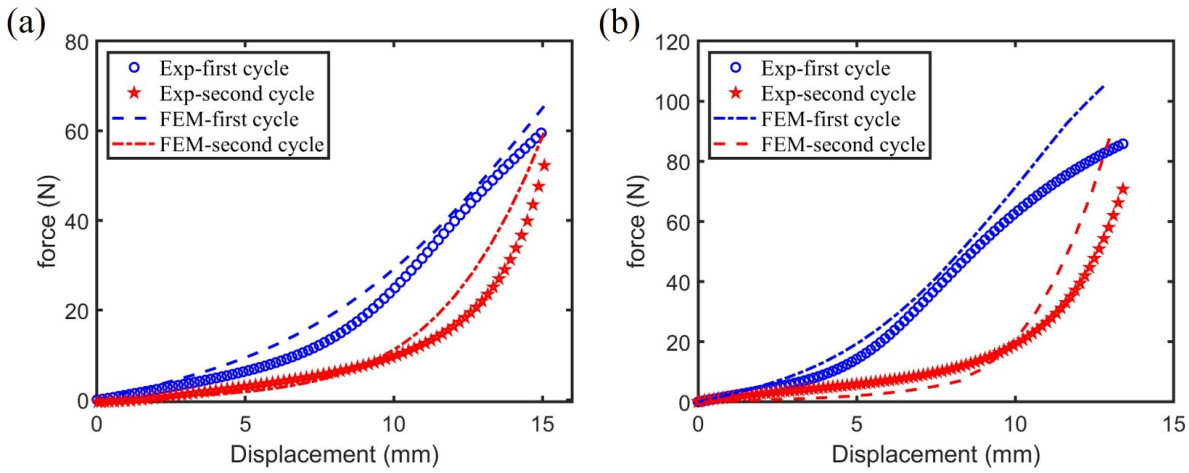

Figure 18: Comparison between experimentally measured and model predicted force–displacement curves for the two loading cycles: (a) pre-holed TN elastomer and (b) pre-cracked TN elastomer.

We compare the experimental (left) and simulated (right) fluorescence maps under various loading conditions for a pre-holed sample with a maximum stretch of 2.0 (Fig. 19 and Fig. 20) and a pre-cracked sample with a maximum stretch of 2.35 (Fig. 21 and Fig. 22), respectively. During the initial loading cycle (Fig. 19 and Fig. 21), fluorescence intensities are clearly localized around both sides of the hole and at the crack tip. Regions closer to the hole or crack tip exhibit higher fluorescence intensities due to stress concentration effects. Owing to symmetric loading conditions,

the experimentally obtained fluorescence maps display a symmetric pattern. During the reloading phase, following unloading and fluorescence fading, fluorescence response differs notably from the initial loading. Specifically, the overall fluorescence intensity distributions (Fig. 20 and Fig. 22) are significantly weaker than in the first loading cycle (Fig. 19 and Fig. 21). This reduction indicates that damage accumulation makes a portion of mechanophores inactivate.

Overall, for both pre-holed and pre-cracked cases, the model successfully captures the spatial and cyclic evolution of mechanochemical response under inhomogeneous loading conditions. This demonstrates that the model can capture the response in both homogenous and inhomogeneous loading conditions.

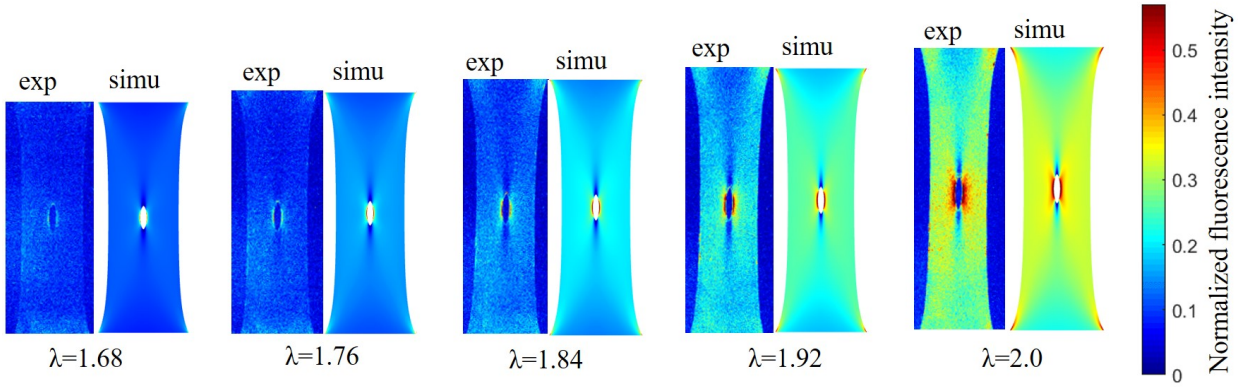

Figure 19: Comparison of simulated (right) and experimental (left) fluorescence images for a circular-hole TN sample in the first loading cycle for different stretch ratios (maximum stretch: 2.0, loading speed: 45 mm/min).

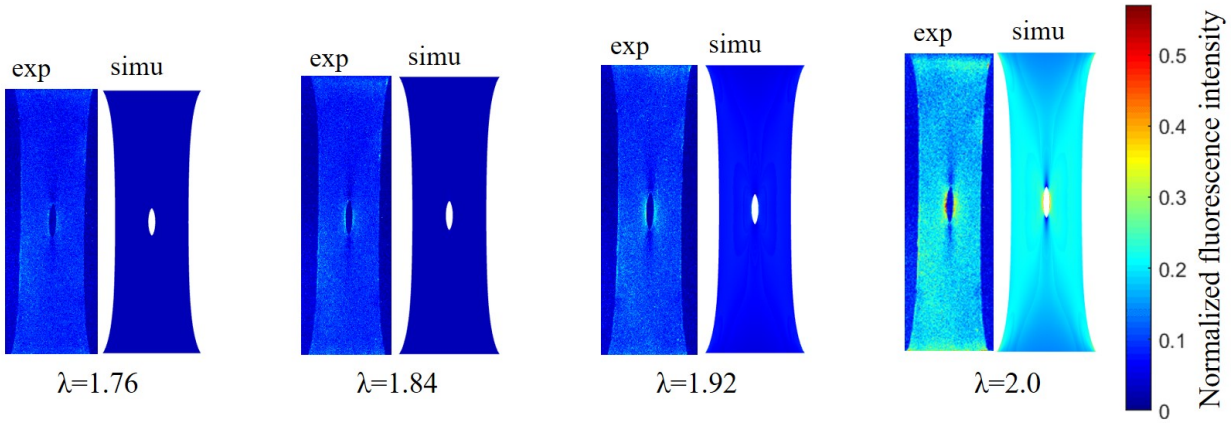

Figure 20: Comparison of simulated (right) and experimental (left) fluorescence images for a circular-hole TN sample in the reloading cycle for different stretch ratios.

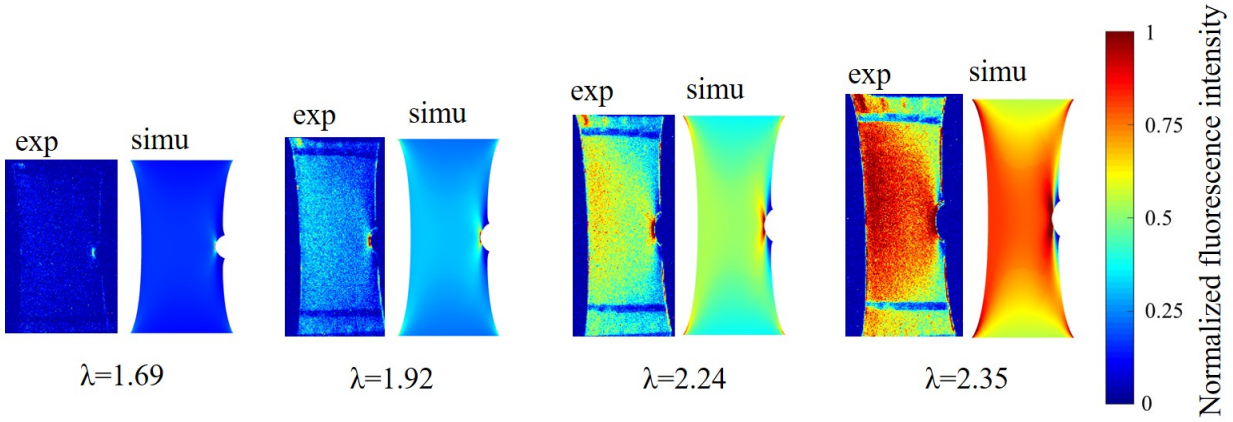

Figure 21: Comparison of simulated (right) and experimental (left) fluorescence images for a pre-cracked TN sample in the first loading cycle for different stretch ratios (maximum stretch: 2.35, loading speed: 30 mm/min).

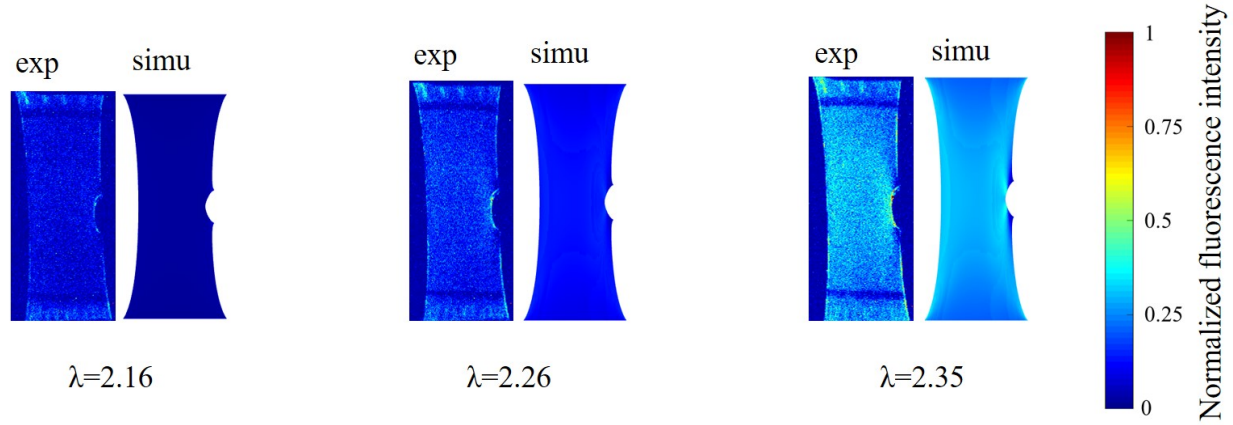

Figure 22: Comparison of simulated (right) and experimental (left) fluorescence images for a pre-cracked TN sample in the reloading cycle for different stretch ratios.

7. Conclusion

In this work, we developed a chemo-mechanical coupled model for mechanofluorescent multiple network elastomers incorporating rhodamine mechanophores. The experimental results have shown a strong coupling between damage and fluorescent response in such materials. Building upon these findings, the model integrates the dynamic theory of mechanophore activation into the damage model of multiple network elastomers. The first network is assumed to exhibit a progressive damage behavior, while the matrix network shows a hyperelastic response. For the mechanochemical modeling, mechanophores linked to the first network are activated when the chain force lies between the critical thresholds for activation and damage. Otherwise, they remain or revert to their inactive states. Through parameter analysis, it is shown that the activation of mechanophores depends on the loading stretch rate as well as forward and backward reaction rates, reflecting the time-dependent nature of the process. Additionally, factors such as the number of chain segments and the normalized critical activation force affect mechanophore activation. By assuming that the total concentration of activated mechanophores is proportional to the macroscopic fluorescence intensity, the model establishes a bridge between molecular-scale activation events and bulk optical signals. The model accurately captures both mechanical and fluorescent response of various multiple network elastomers during loading and reloading tests, showing good agreement with experimental data. Notably, it successfully predicts both the Mullins effect observed in the cyclic loading–unloading tests and the delayed activation phenomenon in fluorescence, both attributed to accumulated damage. Finally, the model predicts the mechanochemical response of TN elastomer samples with inhomogeneous deformation, demonstrating reasonable agreement with experimental fluorescence images. These results confirm that the model can successfully reproduce the coupled mechanical and mechanochemical behavior of mechanofluorescent multiple network elastomers.

Acknowledgments

Rui Xiao acknowledges the Natural Science Foundation of Hangzhou (Grant No. 2024SZRYBB040002), the Fundamental Research Funds for the Central Universities (Grant No. 226-2025-00137), National Natural Science Foundation of China (Grant Nos. 12211530061,12321002), and the 111 Project (Grant No. B21034). Mokarram Hossain acknowledges the Royal Society-NSFC International Exchange Grant (IEC/NSFC/211316) and the support from the Engineering and Physical Sciences Research Council (EPSRC) under the grant (EP/Z535710/1). Paul Steinmann acknowledges support from the European Research Council (ERC) under the Horizon Europe program (Grant -No. 101052785, project: SoftFrac). Funded by the European Union. Views and opinions expressed are however those

of the author(s) only and do not necessarily reflect those of the European Union or the European Research Council Executive Agency. Neither the European Union nor the granting authority can be held responsible for them.

Appendix A. Numerical implementation

For the finite element implementation, the constitutive model is implemented within COMSOL Multiphysics. The mechanical response is formulated using the built-in hyperelastic framework, in which the Helmholtz free energy density is defined in a user-specified form to account for the network contributions. The damage effect is incorporated through updating the chain density P_j. This formulation allows the stress response to be obtained through automatic differentiation of the free energy with respect to the deformation gradient, ensuring numerical robustness and consistency.

Eqs. (19) and (30) govern the evolution of the state variables P_j and c_j^{A}. These equations are solved numerically using the finite difference scheme. Taking Eq. (19) as an example, the forward difference approximation is employed to discretize the time derivative, which allows the evolution of the state variable to be updated incrementally at each time step. When $\overline{f}_j > \overline{f}_{\mathrm{cri}}^{\mathrm{m}}$, the governing equation can be written as

$$\frac{P_j^{(\mathrm{n+1})} - P_j^{(\mathrm{n})}}{\Delta t} = -\frac{N_j P_j^{(\mathrm{n+1})}}{\tau_{\mathrm{a}}} \exp\left(\frac{l_{\mathrm{a}}[\overline{f}_j - \overline{f}_{\mathrm{cri}}^{\mathrm{m}}]}{b}\right), \tag{A.1}$$

where the $P_j^{(\mathrm{n+1})}$ and $P_j^{(\mathrm{n})}$ denote the value of P_j at the n+1-th and n-th time steps, respectively. This expression can be rearranged into the following update form:

$$P_j^{(\mathrm{n+1})} = P_j^{(\mathrm{n})} \frac{1}{1 + \dfrac{N_j \Delta t}{\tau_{\mathrm{a}}} \exp\left(\dfrac{l_{\mathrm{a}}[\overline{f}_j - \overline{f}_{\mathrm{cri}}^{\mathrm{m}}]}{b}\right)}, \quad \text{if } \overline{f}_j > \overline{f}_{\mathrm{cri}}^{\mathrm{m}}. \tag{A.2}$$

It is noted that the multiplicative factor $1/\left[1 + \dfrac{N_j \Delta t}{\tau_{\mathrm{a}}} \exp(\dfrac{l_{\mathrm{a}}[\overline{f}_j - \overline{f}_{\mathrm{cri}}^{\mathrm{m}}]}{b})\right]$ is strictly smaller than unity. Consequently, once the chain force exceeds the critical value, the corresponding chain density P_j decreases monotonically.

Similarly, when $\overline{f}_j \leq \overline{f}_{\mathrm{cri}}^{\mathrm{m}}$, the evolution equation reduces to

$$P_j^{(\mathrm{n+1})} = P_j^{(\mathrm{n})}, \quad \text{if } \overline{f}_j \leq \overline{f}_{\mathrm{cri}}^{\mathrm{m}}, \tag{A.3}$$

indicating that the chain density remains unchanged in this case.

References

Anssari-Benam, A., Bucchi, A., Destrade, M., Saccomandi, G., 2022a. The generalised mooney space for modelling the response of rubber-like materials. Journal of Elasticity 151 (1), 127–141.

Anssari-Benam, A., Destrade, M., Saccomandi, G., 2022b. Modelling brain tissue elasticity with the ogden model and an alternative family of constitutive models. Philosophical Transactions of the Royal Society A 380 (2234), 20210325.

Arruda, E. M., Boyce, M. C., 1993. A three-dimensional constitutive model for the large stretch behavior of rubber elastic materials. Journal of the Mechanics and Physics of Solids 41 (2), 389–412.

Barbee, M. H., Mondal, K., Deng, J. Z., Bharambe, V., Neumann, T. V., Adams, J. J., Boechler, N., Dickey, M. D., Craig, S. L., 2018. Mechanochromic stretchable electronics. ACS applied materials & interfaces 10 (35), 29918–29924.

Beiermann, B. A., Kramer, S. L., May, P. A., Moore, J. S., White, S. R., Sottos, N. R., 2014. The effect of polymer chain alignment and relaxation on force-induced chemical reactions in an elastomer. Advanced Functional Materials 24 (11), 1529–1537.

Buche, M. R., Silberstein, M. N., 2021. Chain breaking in the statistical mechanical constitutive theory of polymer networks. Journal of the Mechanics and Physics of Solids 156, 104593.

Chen, Y., Mellot, G., van Luijk, D., Creton, C., Sijbesma, R. P., 2021a. Mechanochemical tools for polymer materials. Chemical Society Reviews 50 (6), 4100–4140.

Chen, Y., Sanoja, G., Creton, C., 2021b. Mechanochemistry unveils stress transfer during sacrificial bond fracture of tough multiple network elastomers. Chemical science 12 (33), 11098–11108.

Chen, Y., Spiering, A., Karthikeyan, S., Peters, G. W., Meijer, E., Sijbesma, R. P., 2012. Mechanically induced chemiluminescence from polymers incorporating a 1, 2-dioxetane unit in the main chain. Nature chemistry 4 (7), 559–562.

Chen, Y., Yeh, C. J., Qi, Y., Long, R., Creton, C., 2020. From force-responsive molecules to quantifying and mapping stresses in soft materials. Science advances 6 (20), eaaz5093.

Cho, S., Kang, S., Pandya, A., Shanker, R., Khan, Z., Lee, Y., Park, J., Craig, S. L., Ko, H., 2017. Large-area cross-aligned silver nanowire electrodes for flexible, transparent, and force-sensitive mechanochromic touch screens. ACS nano 11 (4), 4346–4357.

Clough, J. M., Creton, C., Craig, S. L., Sijbesma, R. P., 2016. Covalent bond scission in the mullins effect of a filled elastomer: real-time visualization with mechanoluminescence. Advanced Functional Materials 26 (48), 9063–9074.

Dargazany, R., Itskov, M., 2009. A network evolution model for the anisotropic mullins effect in carbon black filled rubbers. International Journal of Solids and Structures 46 (16), 2967–2977.

Davis, D. A., Hamilton, A., Yang, J., Cremar, L. D., Van Gough, D., Potisek, S. L., Ong, M. T., Braun, P. V., Martínez, T. J., White, S. R., et al., 2009. Force-induced activation of covalent bonds in mechanoresponsive polymeric materials. Nature 459 (7243), 68–72.

Ducrot, E., Chen, Y., Bulters, M., Sijbesma, R. P., Creton, C., 2014. Toughening elastomers with sacrificial bonds and watching them break. Science 344 (6180), 186–189.

Eyring, H., Polanyi, M., 1931. Über einfache gasreaktionen. Z. Phys. Chem. B 12, 279–311.

Gossweiler, G. R., Brown, C. L., Hewage, G. B., Sapiro-Gheiler, E., Trautman, W. J., Welshofer, G. W., Craig, S. L., 2015. Mechanochemically active soft robots. ACS applied materials & interfaces 7 (40), 22431–22435.

Göstl, R., Sijbesma, R., 2016. π-extended anthracenes as sensitive probes for mechanical stress. Chemical science 7 (1), 370–375.

Govindjee, S., Simo, J., 1991. A micro-mechanically based continuum damage model for carbon black-filled rubbers incorporating mullins' effect. Journal of the Mechanics and Physics of Solids 39 (1), 87–112.

Jiang, Y., Sun, P., Du, L., Wang, H., Xiao, R., 2025. Puncture of mechanochromic tough elastomeric membranes. Acta Mechanica Solida Sinica, 1–10.

Ju, J., Sanoja, G. E., Nagazi, M. Y., Cipelletti, L., Liu, Z., Hui, C. Y., Ciccotti, M., Narita, T., Creton, C., 2023. Real-time early detection of crack propagation precursors in delayed fracture of soft elastomers. Physical Review X 13 (2), 021030.

Kauzmann, W., Eyring, H., 1940. The viscous flow of large molecules. Journal of the American Chemical Society 62 (11), 3113–3125.

Khiêm, V. N., Itskov, M., 2016. Analytical network-averaging of the tube model:: Rubber elasticity. Journal of the Mechanics and Physics of Solids 95, 254–269.

Kim, T. A., Beiermann, B. A., White, S. R., Sottos, N. R., 2016. Effect of mechanical stress on spiropyran-merocyanine reaction kinetics in a thermoplastic polymer. ACS Macro letters 5 (12), 1312–1316.

Klein, I. M., Husic, C. C., Kovács, D. P., Choquette, N. J., Robb, M. J., 2020. Validation of the cogef method as a predictive tool for polymer mechanochemistry. Journal of the American Chemical Society 142 (38), 16364–16381.

Kroeger, M., 2015. Simple, admissible, and accurate approximants of the inverse langevin and brillouin functions, relevant for strong polymer deformations and flows. Journal of Non-Newtonian Fluid Mechanics 223, 77–87.

Lavoie, S. R., Long, R., Tang, T., 2016. A rate-dependent damage model for elastomers at large strain. Extreme Mechanics Letters 8, 114–124.

Lavoie, S. R., Millereau, P., Creton, C., Long, R., Tang, T., 2019. A continuum model for progressive damage in tough multinetwork elastomers. Journal of the Mechanics and Physics of Solids 125, 523–549.

Lei, J., Liu, Z., 2024. A chain scission-induced anisotropic damage constitutive model for double network hydrogels. International Journal of Applied Mechanics 16 (06), 2450076.

Li, M., Zhang, Q., Zhou, Y.-N., Zhu, S., 2018. Let spiropyran help polymers feel force! Progress in Polymer Science 79, 26–39.

Li, Q., Wang, Q., Yuan, Y., Chen, Y., 2022. Mechanochemiluminescent hydrogels for real-time visualization of chemical bond scission. Synlett 33 (09), 879–884.

Mao, Y., Talamini, B., Anand, L., 2017. Rupture of polymers by chain scission. Extreme Mechanics Letters 13, 17–24.

Marckmann, G., Verron, E., Gornet, L., Chagnon, G., Charrier, P., Fort, P., 2002. A theory of network alteration for the mullins effect. Journal of the Mechanics and Physics of Solids 50 (9), 2011–2028.

Matsuda, T., Kawakami, R., Namba, R., Nakajima, T., Gong, J. P., 2019. Mechanoresponsive self-growing hydrogels inspired by muscle training. Science 363 (6426), 504–508.

Ribas-Arino, J., Marx, D., 2012. Covalent mechanochemistry: theoretical concepts and computational tools with applications to molecular nanomechanics. Chemical reviews 112 (10), 5412–5487.

Silberstein, M. N., Cremar, L. D., Beiermann, B. A., Kramer, S. B., Martinez, T. J., White, S. R., Sottos, N. R., 2014. Modeling mechanophore activation within a viscous rubbery network. Journal of the Mechanics and Physics of Solids 63, 141–153.

Silberstein, M. N., Min, K., Cremar, L. D., Degen, C. M., Martinez, T. J., Aluru, N. R., White, S. R., Sottos, N. R., 2013. Modeling mechanophore activation within a crosslinked glassy matrix. Journal of Applied Physics 114 (2), 023504.

Sun, P., Qu, S., Xiao, R., 2024. On the theory of mechanically induced chemiluminescence in multiple network elastomers. Journal of the Mechanics and Physics of Solids 184, 105543.

Sun, P., Wang, Q., Yang, J., Chen, Y., Wang, Z., Qu, S., Creton, C., Xiao, R., 2025. Quantitative stress and damage mapping in multiple network elastomers using a single mechanophore. Nature Communications 16 (1), 10079.

Vernerey, F. J., Brighenti, R., Long, R., Shen, T., 2018. Statistical damage mechanics of polymer networks. Macromolecules 51 (17), 6609–6622.

Wang, K., Dai, L., Lin, J., Rao, P., Xiao, R., 2024. Mechanical behaviors of copolymer elastomers: Experimental characterization and constitutive modeling. International Journal of Applied Mechanics 16 (06), 2441002.

Wang, Q., Gossweiler, G. R., Craig, S. L., Zhao, X., 2014. Cephalopod-inspired design of electro-mechano-chemically responsive elastomers for on-demand fluorescent patterning. Nature communications 5 (1), 4899.

Wang, Q., Gossweiler, G. R., Craig, S. L., Zhao, X., 2015a. Mechanics of mechanochemically responsive elastomers. Journal of the Mechanics and Physics of Solids 82, 320–344.

Wang, T., Zhang, N., Dai, J., Li, Z., Bai, W., Bai, R., 2017. Novel reversible mechanochromic elastomer with high sensitivity: bond scission and bending-induced multicolor switching. ACS Applied Materials & Interfaces 9 (13), 11874–11881.

Wang, Z., Ma, Z., Wang, Y., Xu, Z., Luo, Y., Wei, Y., Jia, X., 2015b. A novel mechanochromic and photochromic polymer film: when rhodamine joins polyurethane. Advanced Materials 27 (41), 6469–6474.

Wang, Z., Zheng, X., Ouchi, T., Kouznetsova, T. B., Beech, H. K., Av-Ron, S., Matsuda, T., Bowser, B. H., Wang, S., Johnson, J. A., et al., 2021. Toughening hydrogels through force-triggered chemical reactions that lengthen polymer strands. Science 374 (6564), 193–196.

Wang, Z. J., Li, W., Li, X., Nakajima, T., Rubinstein, M., Gong, J. P., 2025. Rapid self-strengthening in double-network hydrogels triggered by bond scission. Nature Materials 24, 607–614.

Webber, R. E., Creton, C., Brown, H. R., Gong, J. P., 2007. Large strain hysteresis and mullins effect of tough double-network hydrogels. Macromolecules 40 (8), 2919–2927.

Wu, M., Li, Y., Yuan, W., De Bo, G., Cao, Y., Chen, Y., 2022. Cooperative and geometry-dependent mechanochromic reactivity through aromatic fusion of two rhodamines in polymers. Journal of the American Chemical Society 144 (37), 17120–17128.

Xiao, R., Han, N., Zhong, D., Qu, S., 2021. Modeling the mechanical behaviors of multiple network elastomers. Mechanics of Materials 161, 103992.

You, J., Zhang, J., Yang, B., Wang, C., Liu, Z., 2025. Damage mechanism insights into double network hydrogels: Predicting cyclic loading behaviors via monotonic loading. Journal of the Mechanics and Physics of Solids 205, 106324.

Zhan, L., Wang, S., Qu, S., Steinmann, P., Xiao, R., 2023a. A general continuum damage model for soft composites. Journal of the Mechanics and Physics of Solids, 105290.

Zhan, L., Wang, S., Qu, S., Steinmann, P., Xiao, R., 2023b. A new micro–macro transition for hyperelastic materials. Journal of the Mechanics and Physics of Solids 171, 105156.

Zhao, Z., Lei, H., Chen, H.-S., Zhang, Q., Wang, P., Lei, M., 2021. A multiscale tensile failure model for double network elastomer composites. Mechanics of Materials 163, 104074.